JOC The Journal of Organic Chemistry

pubs.acs.org/joc Article

Encapsulation of Aromatic Guests in the Bisporphyrin Cavity of a Double-Stranded Spiroborate Helicate: Thermodynamic and Kinetic Studies and the Encapsulation Mechanism

Naoki Ousaka,* Shinya Yamamoto, Hiroki Iida, Takuya Iwata, Shingo Ito, Rafael Souza, Yuh Hijikata,* Stephan Irle, and Eiji Yashima*

Cite This: J. Org. Chem. 2021, 86, 10501−10516 Read Online

ACCESS | Metrics & More | Article Recommendations | Supporting Information

ABSTRACT: A double-stranded spiroborate helicate bearing a bisporphyrin unit in the middle forms an inclusion complex with electron-deficient aromatic guests that are sandwiched between the porphyrins. In the present study, we systematically investigated the effects of size, electron density, and substituents of a series of aromatic guests on inclusion complex formations within the bisporphyrin. The thermodynamic and kinetic behaviors during the guest-encapsulation process were also investigated in detail. The guest-encapsulation abilities in the helicate increased with the increasing core sizes of the electron-deficient aromatic guests and decreased with the increasing bulkiness and number of substituents of the guests. Among the naphthalenediimide derivatives, those with bulky *N*-substituents at both ends hardly formed an inclusion complex. Instead, they formed a [2]rotaxane-like inclusion complex through the water-mediated dynamic B−O bond cleavage/reformation of the spiroborate groups of the helicate, which enhanced the conformational flexibility of the helicate to enlarge the bisporphyrin cavity and form an inclusion complex. Based on the X-ray crystal structure of a unique pacman-like 1:1 inclusion complex between the helicate and an ammonium cation as well as the molecular dynamics simulation results, a plausible mechanism for the inclusion of a planar aromatic guest within the helicate is also proposed.

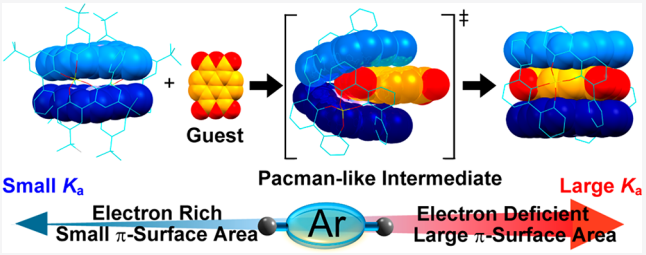

INTRODUCTION

Well-defined three-dimensional structures with specific molecular pockets or cavities are indispensable to enzymes and proteins due to their sophisticated functions to which substrates of a complementary size and shape can bind with an extremely high selectivity and specificity for further transformation reactions, energy or electron transfers, etc. Since the first synthesis of cryptands and cavitands,[1] the development of synthetic receptors that possess an interior space suitable for guest binding has attracted considerable attention because of their numerous applications[2] to sensory systems,[2a,d,e] catalysts,[2f,g] nanoreactors,[2b] and ion transporters.[2c−h] Among such artificial receptors, the bisporphyrin-based receptors[2f,3] that are composed of two porphyrins[4] or their metalated derivatives and are linked by one,[5] two,[6] or more[6e,7] flexible or rigid linkages of varying lengths are particularly interesting because of the unique nanospace created between the two (metallo)porphyrins with their large π-delocalized cores. This nanospace enables the encapsulation of not only various π-conjugated guest molecules,[5b,e,6d,f−i,7b,c] fullerenes,[5d,6b,e,7d] and carbon nanotubes[5h] through intermolecular π−π stacking interactions but also a variety of chiral[5a,c,f,g,7d] and achiral bidentate ligands[6a,c,7a] through metal−ligand interactions.[3b,c,f,i]

We recently found that a double-stranded spiroborate helicate bearing a bisporphyrin unit in the middle ($\mathbf{1}_{X2}$: X = Na^+ or tetra-*n*-butylammonium (TBA^+)) formed an inclusion complex with an electron-deficient aromatic guest, such as **G4** ($\mathbf{1}_{X2}\supset$**G4**) (Figure 1a), in such a way that the bisporphyrin sandwiched the guest in a parallel manner was largely stabilized by face-to-face π-stacking.[6g] Interestingly, this guest encapsulation triggered the quite unique rotary motion of the porphyrin rings in one direction, which was coupled with a unidirectional twisting motion of the spiroborate helix.[6g,8,9] The right- (*P*) and left-handed (*M*) enantiomers of $\mathbf{1}_{X2}$ were readily obtained by the optical resolution of the racemic bisporphyrin helicate through diastereomeric salt formation with an enantiopure ammonium, followed by cation exchanges with achiral ammoniums.[6g] In addition, the enantiopure one-handed $\mathbf{1}_{TBA2}$ was able to selectively include one of the

Received: May 18, 2021
Published: July 20, 2021

https://doi.org/10.1021/acs.joc.1c01155
J. Org. Chem. 2021, 86, 10501−10516

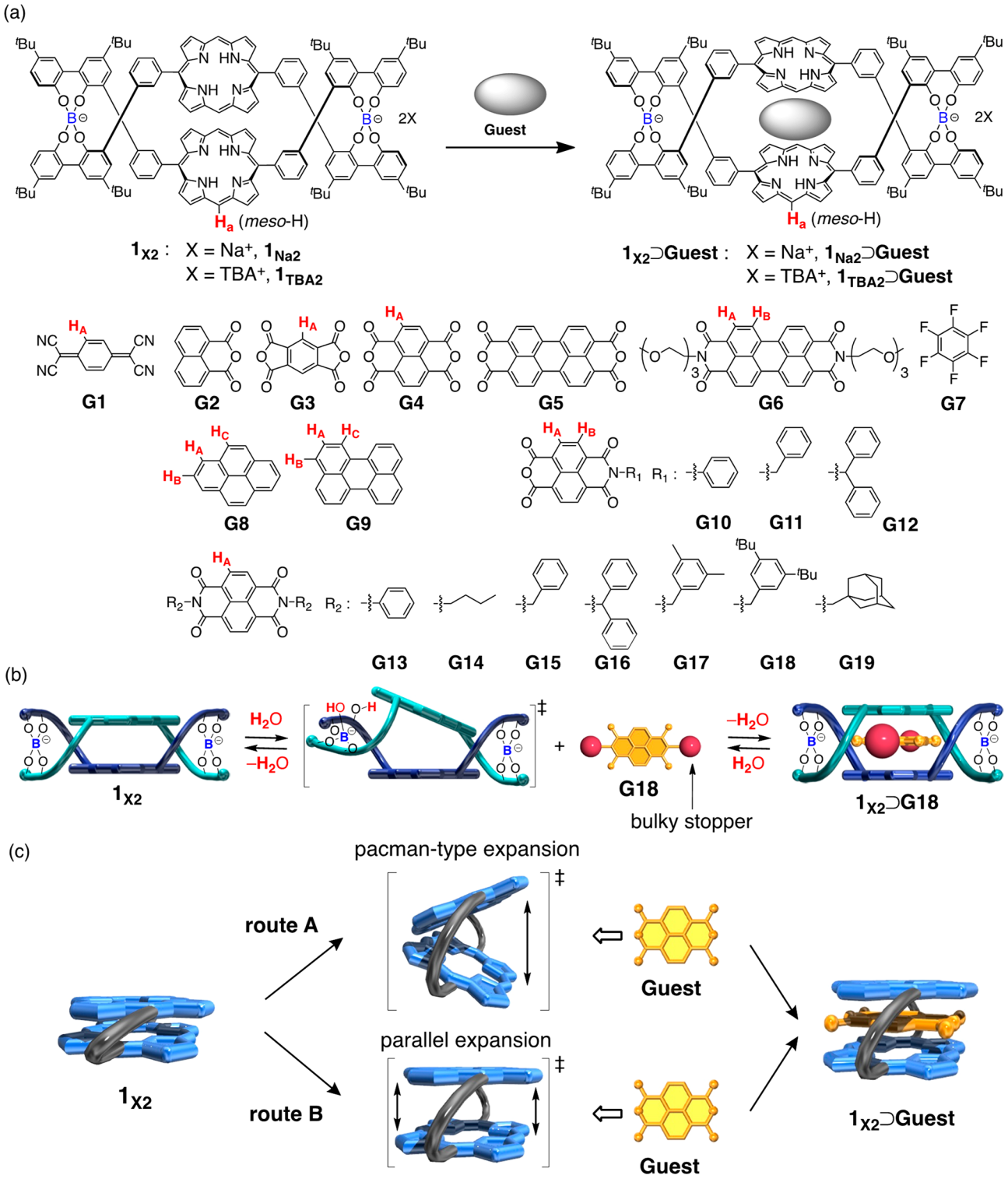

Figure 1. (a) Chemical structures of $\mathbf{1}_{X2}$ (X = Na^+ or TBA^+) and **G1**−**G19** and the inclusion complexation of $\mathbf{1}_{X2}$ with various guests. (b) Schematic representation of a plausible mechanism for the inclusion of **G18** bearing bulky stoppers at both ends in the bisporphyrin helicate $\mathbf{1}_{X2}$ through the reversible B−O bond cleavage/reformation of the spiroborate groups. The bulky stoppers of **G18** are possible to pass through the bisporphyrin cavity of $\mathbf{1}_{X2}$ only when the inner cavity of $\mathbf{1}_{X2}$ is temporarily expanded by the water-mediated B−O bond cleavages of the spiroborate groups (see Figure 4). (c) Schematic representation of two possible mechanisms (routes A and B) for the guest encapsulation in the bisporphyrin cavity of $\mathbf{1}_{X2}$.

enantiomers of a racemic naphthalenemonoimide (NMI) derivative with a chiral aromatic substituent at one end through efficient edge-to-face CH−π interactions between the bisporphyrin residue and an aromatic group of the encapsulated chiral guest.[6i] Moreover, the racemic $\mathbf{1}_{Na2}$ underwent a unique deracemization reaction upon complexation with an enantiopure electron-deficient NMI-based aromatic guest through the water-mediated B−O bond

https://doi.org/10.1021/acs.joc.1c01155
J. Org. Chem. 2021, 86, 10501−10516

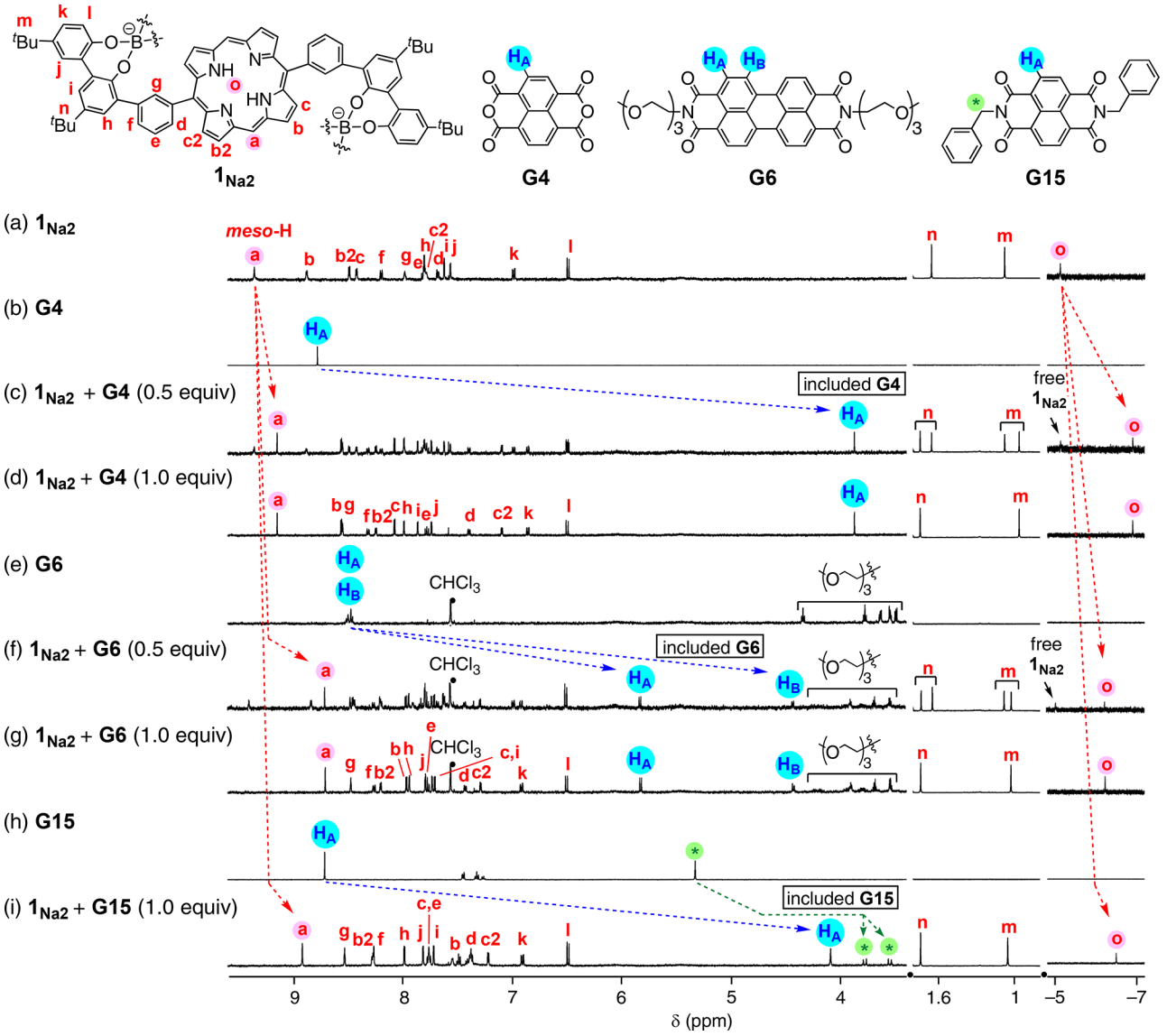

Figure 2. Partial ^{1}H NMR spectra (500 MHz, CD_3CN, 25 °C) of (a) $\mathbf{1}_{Na2}$ (0.2 mM), (b) **G4** (0.5 mM), $\mathbf{1}_{Na2}$ plus (c) 0.5 and (d) 1.0 equiv of **G4**, (e) **G6** (0.1 mM in $CD_3CN/CDCl_3$ (5/2 v/v)), $\mathbf{1}_{Na2}$ plus (f) 0.5 and (g) 1.0 equiv of **G6** ($CD_3CN/CDCl_3$ (5/2 v/v)), (h) **G15** (0.5 mM), and (i) $\mathbf{1}_{Na2}$ plus 1.0 equiv of **G15**. For the signal assignments of $\mathbf{1}_{Na2}$ in the presence of 1.0 equiv of **G6** and **G15**, see Figures S37−S40. The signal assignments of $\mathbf{1}_{Na2}$ and $\mathbf{1}_{Na2}$ plus 1.0 equiv of **G4** were previously reported.[6g]

cleavage/reformation of the spiroborate groups, thus producing a nonracemic helicate.[6i]

However, the thermodynamic and kinetic stabilities of the inclusion complexes of $\mathbf{1}_{Na2}$ toward electron-deficient aromatic guests, the inclusion and release kinetics of $\mathbf{1}_{Na2}$, and the mechanistic insight into the guest inclusion complexation process of $\mathbf{1}_{Na2}$[6g] are poorly understood. Herein we report our comprehensively investigated results of the inclusion complexation behaviors between $\mathbf{1}_{Na2}$ and a series of planar aromatic guests with various sizes, substituents, and electron densities (Figure 1a). Among the various tested guests, a naphthalenediimide (NDI) derivative bearing bulky stoppers at both ends, such as **G18**, was found to be included in $\mathbf{1}_{Na2}$ to form a stable [2]rotaxane-like complex through the unique water-mediated dynamic B−O bond cleavage/reformation of the spiroborate groups (Figure 1b). Moreover, a plausible mechanism for the inclusion of a planar electron-deficient aromatic guest within the bisporphyrin cavity of the helicate is also proposed on the basis of molecular dynamics (MD) simulation results and the X-ray crystal structure of a pacman-like 1:1 inclusion complex between the helicate and a bulky quaternary ammonium cation, which is considered to be a possible intermediate relevant to the encapsulation mechanism of aromatic guests in the present bisporphyrin helicate as well as the reported bisporphyrin-based host molecules (Figure 1c).

RESULTS AND DISCUSSION

Encapsulation of Various Aromatic Guests in the Helicate. The racemic spiroborate helicate $\mathbf{1}_{Na2}$ and its (*M*)-double-helical enantiomer complexed with achiral TBA ((*M*)-$\mathbf{1}_{TBA2}$) were prepared according to a previously reported method.[6g] Aromatic guests were either commercially available or synthesized according to the literature or procedures in section 2 of the Supporting Information (SI).

We first investigated the binding affinity of $\mathbf{1}_{Na2}$ toward a series of planar aromatic guests (**G1**−**G9**), which were

https://doi.org/10.1021/acs.joc.1c01155
J. Org. Chem. 2021, 86, 10501−10516

Table 1. Association Constants (K_a) of Guests (G1−G19) with $\mathbf{1}_{Na2}$ and the Complexation-Induced ^{1}H Chemical Shift Changes ($\Delta\delta_G$) of Guests G1−G19 in CD_3CN at 25 °C

guest	K_a (M^{-1})	$\Delta\delta_G$ (ppm)[a]	$\Delta\delta(H_A-H_B)$ (ppm)[b]	$\Delta\delta_{NH}$ (ppm)[c]	$\Delta\delta_{meso\text{-}H}$ (ppm)[d]
G1	$(2.5 \pm 0.2) \times 10^5$	8.71 (H_A)		0.54	0.11
G2	$(1.3 \pm 0.1) \times 10^5$	n.a.[e]		1.75	0.26
G3	$(3.7 \pm 0.1) \times 10^5$	8.56 (H_A)		1.21	0.25
G4	$(2.2 \pm 0.3) \times 10^9$	4.91 (H_A)		1.92	0.25
G5	n.a.[f]	n.a.[f]		1.29	0.58
G6	$(1.8 \pm 0.2) \times 10^9$	2.66 (H_A),[g] 4.05 (H_B)[g]	1.39	1.14[h]	0.68[h]
G7	$(3.1 \pm 0.1) \times 10^2$				
G8	n.a.[i]	0.05 (H_A), 0.05 (H_B), 0.05 (H_C)			
G9	n.a.[i]	0.34 (H_A), 0.25 (H_B), 0.74 (H_C)			
G10	$(6.0 \pm 0.6) \times 10^7$	5.21 (H_A), 4.23 (H_B)	0.98	1.65, 1.60	0.22, 0.13
G11	$(9.6 \pm 0.5) \times 10^7$	5.32 (H_A), 4.30 (H_B)	1.02	2.02, 1.92	0.65, 0.21
G12	$(2.3 \pm 0.1) \times 10^6$	5.58 (H_A), 3.36 (H_B)	1.99	1.56, 1.48	1.00, 0.15
G13	$(2.7 \pm 0.1) \times 10^4$	4.34 (H_A)		1.15	0.01
G14	$(5.2 \pm 0.6) \times 10^5$	4.54 (H_A)		1.50	0.33
G15	$(2.0 \pm 0.1) \times 10^5$	4.62 (H_A)		1.48	0.48
G16	~0[j]	n.a.[j]			
G17	n.a.[f]	4.69 (H_A)		1.42	0.55
G18	~0[j]	4.63 (H_A)[k]		1.58[k]	0.91[k]
G19	~0[j]	n.a.[j]			

[a] $\Delta\delta_G = |\delta_{free\text{-}guest\text{-}HX} - \delta_{included\text{-}guest\text{-}HX}|$, where X = A, B, or C for H_X; see Figure 1a. [b] $\delta(H_A-H_B) = |\delta_{included\text{-}guest\text{-}HA} - \delta_{included\text{-}guest\text{-}HB}|$. [c] $\delta_{NH} = |\delta_{free\text{-}1\text{-}NH} - \delta_{complex\text{-}1\text{-}NH}|$. [d] $\delta_{meso\text{-}H} = |\delta_{free\text{-}1\text{-}meso\text{-}H} - \delta_{complex\text{-}1\text{-}meso\text{-}H}|$. For *meso*-H, see Figure 1a. [e] Could not be obtained due to the broadening of the peaks of the included **G2**. [f] Could not be estimated because of poor solubility of the guest in CD_3CN. [g] In $CD_3CN/CDCl_3$ = 5:2 (v/v). [h] $\delta_{meso\text{-}H} = |\delta_{free\text{-}1\text{-}meso\text{-}H}$ (in CD_3CN) − $\delta_{complex\text{-}1\text{-}meso\text{-}H}$ (in $CD_3CN/CDCl_3$ = 5:2 (v/v))|. [i] Too small to be estimated. [j] **G16**, **G18**, and **G19** could not form inclusion complexes with $\mathbf{1}_{Na2}$ at 25 °C due to their bulky substituents. [k] After heating at 80 °C for 1 week.

composed of different aromatic cores with different electron densities (Figure 1a). The 1:1 inclusion complexations of $\mathbf{1}_{Na2}$ with **G1** and **G4** were previously confirmed by ^{1}H NMR spectroscopy in combination with absorption or fluorescent titrations and were further revealed by X-ray single crystal analysis and electrospray ionization mass spectrometry for **G4**.[6g] Similarly, the helicate $\mathbf{1}_{Na2}$ also formed a 1:1 inclusion complex with the other guests except for the electron-rich **G8** and **G9**, as confirmed by ^{1}H NMR spectroscopy and absorption or fluorescent titrations (see sections 3 and 4 in the SI and below). Panels c and f of Figure 2 show the typical ^{1}H NMR spectra of $\mathbf{1}_{Na2}$ in the presence of 0.5 equiv of the electron-deficient naphthalene- (**G4**) and perylene-based (**G6**) guests in CD_3CN at 25 °C, respectively. The spectra exhibited two sets of signals, which were assigned to the free $\mathbf{1}_{Na2}$ and its inclusion complexes due to a slow exchange between them on the present NMR time scale at 25 °C and were accompanied by significant upfield shifts of the aromatic protons of the guests (H_A and H_B) and those of $\mathbf{1}_{Na2}$. The further addition of the guests (1.0 equiv) quantitatively produced the 1:1 inclusion complexes $\mathbf{1}_{Na2}\supset$**G4** and $\mathbf{1}_{Na2}\supset$**G6** (Figure 2d and g, respectively) (see below for a more detailed discussion of the inclusion complex formations by ^{1}H NMR).

The association constants (K_a) of $\mathbf{1}_{Na2}$ with **G1** and **G4** previously estimated by absorption or fluorescence titrations in CH_3CN at 25 °C were ca. 2.5×10^5 and ca. 2.2×10^9 M^{-1}, respectively (Table 1).[6g] During the fluorescence titrations, we confirmed that the dynamic quenching process of the helicate by an NMI derivative bearing a chiral aromatic substituent at one end (an analogue of **G11**) was negligible and the static quenching process was dominant based on the Stern−Volmer plot of the helicate that was quenched by **G11**, showing the complete linear plot.[6i] Therefore, for the other aromatic guests, the static quenching process might be dominant. The observed difference in their K_a values is presumably due to the difference in their aromatic π-surface areas that are capable of interacting with the electron-rich porphyrin rings, through which $\mathbf{1}_{Na2}$ more efficiently formed a sandwich complex with electron-deficient aromatic guests in a face-to-face parallel manner. Therefore, the K_a values of $\mathbf{1}_{Na2}$ with the less electron-deficient **G2** and **G3** with small π-surface areas ($K_a = 1.3 \times 10^5$ and 3.7×10^5 M^{-1}, respectively) were four orders of magnitude lower than that with **G4** (Table 1 and section 4 in the SI). A further decrease in the K_a value (ca. 3.1×10^2 M^{-1}, Table 1) was observed for hexafluorobenzene (**G7**) despite the electron-deficient nature of its fully substituted benzene ring with the electron-withdrawing (EW) fluoro atoms, which was due to electrostatic repulsion between the electron-rich porphyrin rings of $\mathbf{1}_{Na2}$ and the peripheral fluoro-substituents of **G7**.[6f]

An electron-deficient perylene diimide (PDI) guest (**G6**) carrying two EW triethylene glycol (Tg)-bound imide groups with an aromatic surface area larger than that of **G4** was efficiently included in $\mathbf{1}_{Na2}$ by intercalation, with the high K_a value of ca. 1.8×10^9 M^{-1} that is comparable to that of **G4** (Table 1).[10] The X-ray single-crystal structure of the $\mathbf{1}_{Na2}\supset$**G4** inclusion complex revealed that the bisporphyrin cavity is almost filled with **G4**[6g] so that both the imide terminal moieties of the larger PDI unit of **G6** stick out from the bisporphyrin cavity.[11] As anticipated, electron-rich aromatic guests, such as pyrene (**G8**) and perylene (**G9**), could not be efficiently sandwiched between the bisporphyrin unit of $\mathbf{1}_{Na2}$, as indicated by the negligible changes in their ^{1}H NMR spectra upon mixing with $\mathbf{1}_{Na2}$ (Table 1 and Figures S10 and S11).

Next, we investigated the effects of the imide substituents of NMI (**G10**−**G12**) and NDI (**G13**−**G19**) guests on their binding affinity toward $\mathbf{1}_{Na2}$.[12] As expected, the K_a values were highly dependent on the bulkiness and number of the substituents of the guests and were lower than that of **G4**

https://doi.org/10.1021/acs.joc.1c01155
J. Org. Chem. 2021, 86, 10501−10516

(ca. 2.2 × 10^9 M^{-1}), thus decreasing with the increasing steric repulsion between the imide substituents and bisporphyrin during the inclusion complexation. The K_a values (from ca. 2.7 × 10^4 to ca. 9.6 × 10^7 M^{-1}) decreased in the following order: **G11** > **G10** > **G12** > **G14** > **G15** > **G13** (Table 1).

Thermodynamic Studies of Guest Encapsulations. The temperature-dependent inclusion complex formations of $\mathbf{1}_{Na2}$ toward selected guests composed of different cores or substituents, such as **G3**, **G4**, **G10**, and **G13**, were then studied in CH_3CN to estimate the thermodynamic parameters using the van't Hoff plots of the K_a values, which were obtained by absorption or fluorescence titrations (Figure S3), and the results are summarized in Table 2. The observed negative

Table 2. Thermodynamic Parameters for the Inclusion Complexation of $\mathbf{1}_{Na2}$ with Various Aromatic Guests in CH_3CN[a]

guest	$\Delta G°_{298}$ (kJ mol^{-1})	$\Delta H°$ (kJ mol^{-1})	$T\Delta S°$ (kJ mol^{-1} at 298 K)
G3	−31.5 ± 3.3	−36.3 ± 1.6	−4.8 ± 1.6
G4	−54.1 ± 7.4	−71.8 ± 3.8	−17.6 ± 3.7
G10	−45.0 ± 5.9	−74.1 ± 3.0	−29.5 ± 2.9
G13	−25.3 ± 1.5	−41.2 ± 0.7	−15.9 ± 0.7

[a]The thermodynamic parameters ($\Delta H°$, $\Delta S°$, and $\Delta G°_{298}$) were estimated according to the following equation: $\ln K_a = -(\Delta H°/R)(1/T) + (\Delta S°/R)$.

enthalpy and entropy values clearly indicate that the present inclusion complexation is enthalpy-driven and entropically disfavored as anticipated, since the electron-rich bisporphyrin unit of $\mathbf{1}_{Na2}$ sandwiches the electron-deficient aromatic guests through face-to-face double π−π stacking interactions. These result in a significant expansion between the porphyrin rings, thereby substantially restricting the conformational freedom of both the host and the guest. The $\Delta H°$ values for **G4** and **G10** were similar to each other, but the $T\Delta S°$ value for an NMI derivative **G10** was more negative than that for **G4** as a result of the additional restricted molecular motion with respect to that of the pendant phenyl group of the included **G10**. However, both the negative $T\Delta S°$ and $\Delta H°$ values for the NDI derivative **G13** carrying two phenyl substituents were approximately half the values for **G10** (Table 2), suggesting an inefficient π−π stacking interaction between the NDI core of **G13** and the bisporphyrin that resulted from the increased steric repulsion between the pendant phenyl groups of **G13** and the bisporphyrin unit of $\mathbf{1}_{Na2}$; therefore, its K_a value at 25 °C was three orders of magnitude lower than that of **G10**.

Encapsulation of Bulky Guests via Water-Mediated B−O Bond Cleavage/Reformation of the Spiroborate Groups of the Helicate. In sharp contrast to the NDI guests **G13**−**G15** and **G17**, which had relatively small imide substituents, those with bulky substituents at both ends, such as the diphenylmethyl (**G16**), 3,5-di-*tert*-butylbenzyl (**G18**), and 1-adamantylmethyl (**G19**) groups, hardly formed inclusion complexes with $\mathbf{1}_{Na2}$ in either CD_3CN or a $CD_3CN/CDCl_3$ mixture (5:2 v/v) at room temperature (Figures S18a−c, S20a−c, and S21a−c, respectively), indicating that these imide substituents were too sterically hindered to form a stable 1:1 inclusion complex or too bulky to pass through the bisporphyrin cavity of $\mathbf{1}_{Na2}$. Similar behavior was also previously observed for a PDI derivative bearing a bulky 3,5-di-*tert*-butylbenzyl stopper at both ends, which was unable to form an inclusion complex with $\mathbf{1}_{Na2}$ at room temperature because of the bulky stoppers.[6h]

On the other hand, we have recently found that optically active (*M*)-$\mathbf{1}_{TBA2}$, which is kinetically inert toward racemization in the absence of water, readily racemizes in organic solvents in the presence of water through the water-mediated B−O bond cleavage/reformation of the spiroborate groups of $\mathbf{1}_{Na2}$.[6i] These results provided a promising approach for producing an inclusion complex of $\mathbf{1}_{Na2}$ with even bulky **G16**, **G18**, and **G19** guests in aqueous solvents in which the water-mediated B−O bond cleavages of the spiroborate groups could be promoted, resulting in an enhancement of the conformational flexibility of $\mathbf{1}_{Na2}$ to enlarge the bisporphyrin cavity and forming a [2]rotaxane-like inclusion complex after the subsequent reformation of the B−O spiroborate bonds.

With this expectation in mind, a 1:1 mixture of $\mathbf{1}_{Na2}$ and **G18** in CD_3CN that contained a large excess of water (ca. 220 equiv) was heated at 80 °C for 92 h or 1 week, affording the desired [2]rotaxane complex $\mathbf{1}_{Na2}\supset$**G18** in a 68% (Figure S22c and d) or almost quantitative yield (Figure S20d), respectively. Meanwhile, no trace amount of the inclusion complex was formed for **G16** and **G19** after being heated at 80 °C for 1 week, indicating that the imide substituents of **G16** (diphenylmethyl group) and **G19** (1-adamantyl group) were too bulky to form a sandwich complex with $\mathbf{1}_{Na2}$ (Figures S18d and S21d). We noted that a similar water-mediated inclusion complex formation hardly proceeded in the presence of a tiny amount of water in CH_3CN (<5 equiv), giving $\mathbf{1}_{Na2}\supset$**G18** in only a 4% yield upon heating at 80 °C for 92 h (Figure S22a,b). These observations clearly indicated that the encapsulation of the bulky guests, such as **G18** bearing bulky stoppers in the macrocyclic bisporphyrin cavity of $\mathbf{1}_{Na2}$, most likely proceeds through the water-mediated B−O bond cleavage of the spiroborate groups, followed by reformation (Figure 1b).

The second-order rate constants (k, M^{-1} s^{-1}) for the formation of $\mathbf{1}_{Na2}\supset$**G18** in the presence of a large excess of water (220 equiv) were then estimated from the slopes of the linear plots of $1/[\mathbf{1}_{Na2}]$ versus time at different temperatures (50−80 °C), which provided the following activation parameters from the Arrhenius and Eyring plots of the kinetic data (Figure S23): E_a = 43.2 kJ mol^{-1}, $\Delta G^{‡}_{298}$ = 86.6 kJ mol^{-1}, $\Delta H^{‡}$ = 40.4 kJ mol^{-1}, and $T\Delta S^{‡}$ = −46.2 kJ mol^{-1} (T = 298 K). These kinetic and thermodynamic parameters, however, would be influenced by the water content.

Interestingly, when the enantiopure (*M*)-$\mathbf{1}_{TBA2}$ was used instead of the racemic $\mathbf{1}_{Na2}$, the resulting inclusion complex $\mathbf{1}_{TBA2}\supset$**G18** (22%) maintained its optical activity (34% enantiomeric excess (ee)) after being heated at 70 °C for 114 h, while the remaining free $\mathbf{1}_{TBA2}$ (78%) almost lost its optical activity (4% ee) (Figure 3).[13] This difference in the optical activities of $\mathbf{1}_{TBA2}$ in its free and included forms, which was derived from (*M*)-$\mathbf{1}_{TBA2}$, suggested that the racemization of (*M*)-$\mathbf{1}_{TBA2}$ was significantly suppressed once complexation occurred with **G18**. Considering this result, two plausible mechanisms for the inclusion complexation of the bulky **G18** in the bisporphyrin cavity (A) with and (B) without the racemization of the helicate (*M*)-$\mathbf{1}_{TBA2}$ through the reversible water-mediated B−O bond cleavage/reformation of the spiroborate groups can be proposed, as shown in Figure 4. The water-mediated racemization of the spiroborate (*M*)-$\mathbf{1}_{TBA2}$ takes place through an inversion of the helicity, which requires at least the simultaneous cleavage of one of the four B−O

https://doi.org/10.1021/acs.joc.1c01155
J. Org. Chem. 2021, 86, 10501−10516

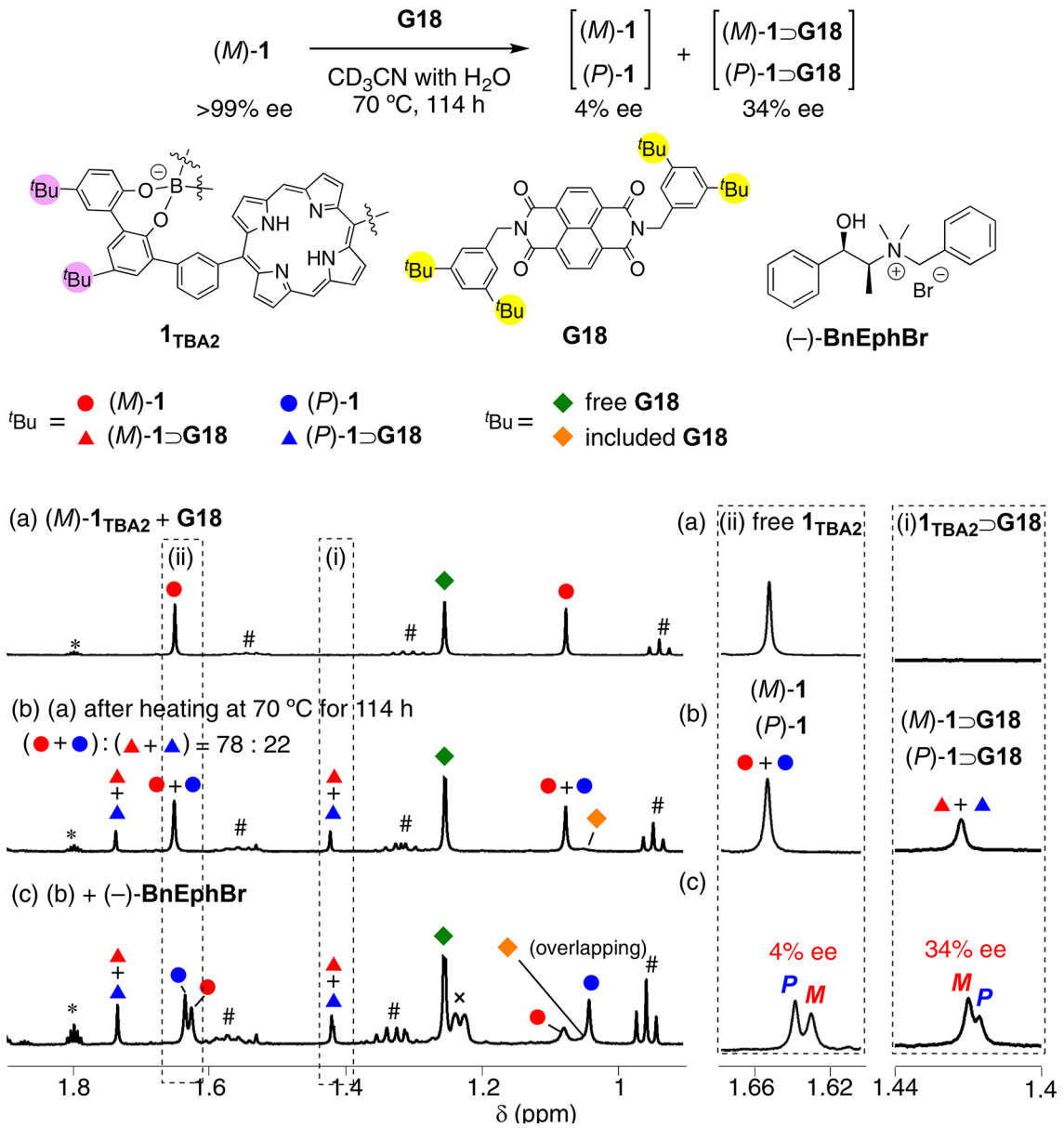

Figure 3. Partial ^{1}H NMR spectra of an equimolar mixture of (*M*)-$\mathbf{1}_{TBA2}$ and **G18** in CD_3CN measured at 25 °C with a small amount of water (a) before and (b) after heating at 70 °C for 114 h and (c) after the addition of 10 equiv of (−)-**BnEphBr**; $(M)\text{-}\mathbf{1}_{TBA2}]_0 = [\mathbf{G18}]_0$ = 0.10 mM and $[H_2O]/[\mathbf{1}_{TBA2}]$ = ca. 0.60. The ee values of free $\mathbf{1}_{TBA2}$ and $\mathbf{1}_{TBA2}\supset\mathbf{G18}$ in panel c were estimated by the integral ratios between the diastereomeric signals in the presence of 10 equiv of (−)-**BnEphBr**, which was used as a chiral shift reagent. The following symbols denote the ^{13}C satellite peaks of the solvent and the protons from TBA and (−)-**BnEphBr**, respectively: *, #, and ×.

bonds at each spiroborate group, probably through the formation of an achiral *meso*-intermediate,[8c] followed by the reformation of the spiroborate groups to produce the racemic free $\mathbf{1}_{TBA2}$ and then its racemic inclusion complex with **G18** ($\mathbf{1}_{TBA2}\supset\mathbf{G18}$) (Figure 4A). On the other hand, the bond cleavage of one or more B−O bond at only one of the two spiroborate groups of (*M*)-$\mathbf{1}_{TBA2}$ allows the helicate to retain its handedness (no racemization) and further allows the bulky stopper groups of **G18** to pass through the enlarged bisporphyrin cavity, leading to inclusion complex formation ((*M*)-$\mathbf{1}_{TBA2}\supset\mathbf{G18}$) while maintaining its one-handed helicity (Figure 4B). These two mechanisms appear to proceed during the inclusion complex formation of **G18** with (*M*)-$\mathbf{1}_{TBA2}$ in CD_3CN containing water (0.6 equiv) at 70 °C, thus producing the almost racemic free $\mathbf{1}_{TBA2}$ via pathway A and its complex ($\mathbf{1}_{TBA2}\supset\mathbf{G18}$) with optical activity through both pathways A and B (Figure 4).[14]

Mechanism of Guest Encapsulation in the Helicate. The X-ray crystallographic analysis of the $\mathbf{1}_{BTMA2}$ (BTMA = benzyltrimethylammonium) single crystals grown by the slow evaporation of an acetone solution of $\mathbf{1}_{Na2}$ in the presence of 5 equiv of BTMA bromide revealed that $\mathbf{1}_{BTMA2}$ adopted a unique pacman-like structure[15] in which one of the two bulky BTMA cations was encapsulated within the cleft of the bisporphyrin, which was composed of two porphyrin rings tilted by ca. 55° (Figures 5 and S24). This pacman-like structure has frequently been observed in a number of cofacial bisporphyrins that are anchored by a single rigid pillar or spacer, but to the best of our knowledge has not been reported in doubly bridged bisporphyrins like $\mathbf{1}_{Na2}$.[15] The observed

https://doi.org/10.1021/acs.joc.1c01155
J. Org. Chem. 2021, 86, 10501−10516

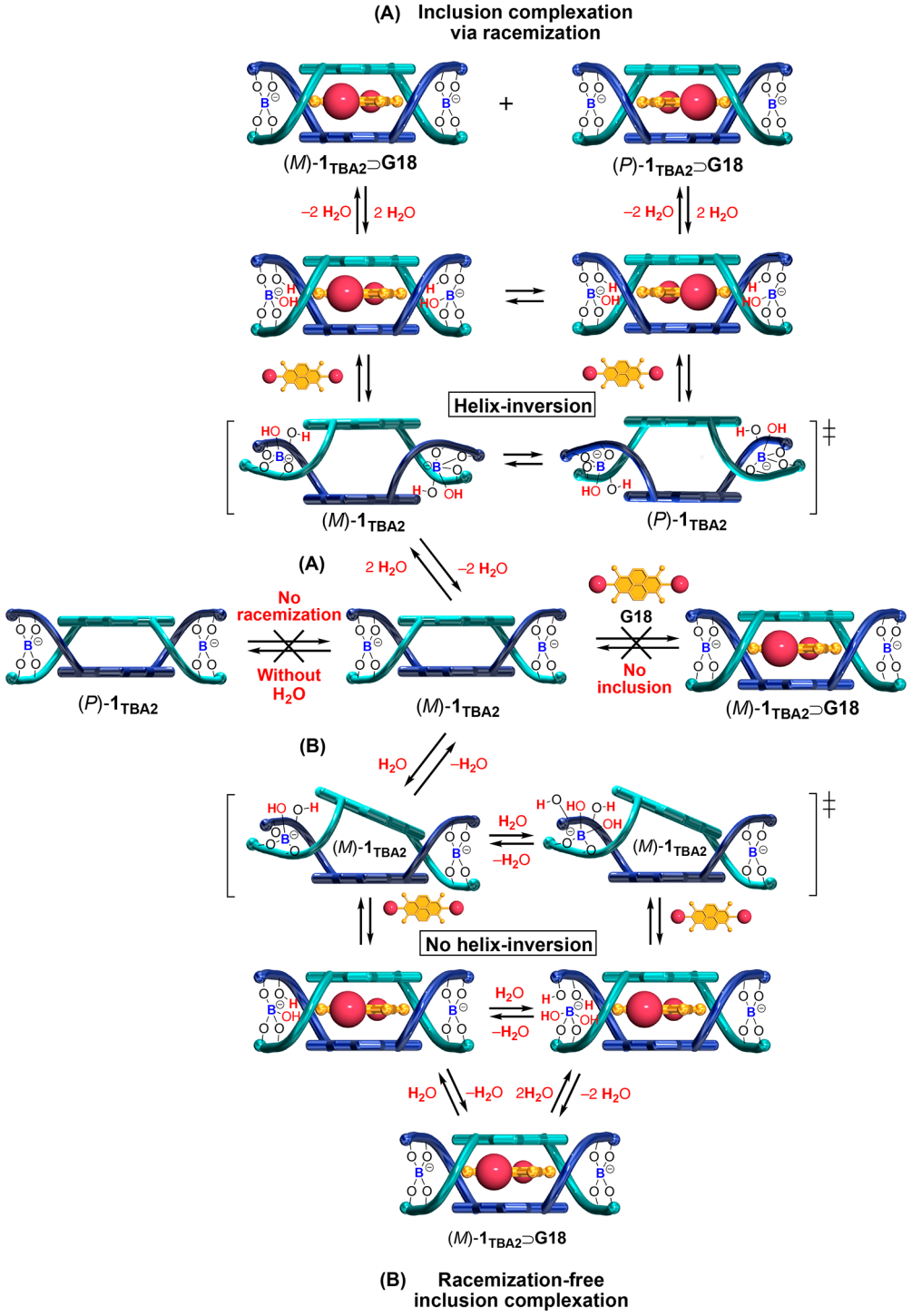

Figure 4. Schematic representation of two plausible pathways for the inclusion of a bulky guest **G18** in the bisporphyrin helicate (*M*)-$\mathbf{1}_{TBA2}$ (A) with and (B) without the racemization of (*M*)-$\mathbf{1}_{TBA2}$ through the reversible B−O bond cleavage/reformation of the spiroborate groups. The inclusion complexation of (*M*)-$\mathbf{1}_{TBA2}$ with **G18** bearing bulky substituents at both ends is possible only when the inner cavity of (*M*)-$\mathbf{1}_{TBA2}$ is temporarily expanded by the water-mediated reversible B−O bond cleavage/reformation of the spiroborate groups. The racemization of (*M*)-$\mathbf{1}_{TBA2}$ takes place during the simultaneous cleavage of one of the four B−O bonds at each spiroborate group (panel A).

unique pacman structure is most likely formed through an induced-fit mechanism driven by cation−π interactions, which are probably cation−quadrupole interactions between the π electron-rich bisporphyrin of $\mathbf{1}^{2-}$ and the cationic methonium group of BTMA.[16] A long-range electrostatic ion−ion interaction between the cationic methonium group of BTMA and the negatively charged borate ions of $\mathbf{1}^{2-}$ as well as solvophobic (CH−π) interactions between the bulky trimethylammonium group of BTMA and the bisporphyrin units of the helicate may also contribute to enhance the stability of the pacman formation, at least in the solid state.[17] The solid-state structure is quite unique and different from the crystal structures of $\mathbf{1}_{Na2}$ and its inclusion complex with **G4**, as

https://doi.org/10.1021/acs.joc.1c01155
J. Org. Chem. 2021, 86, 10501−10516

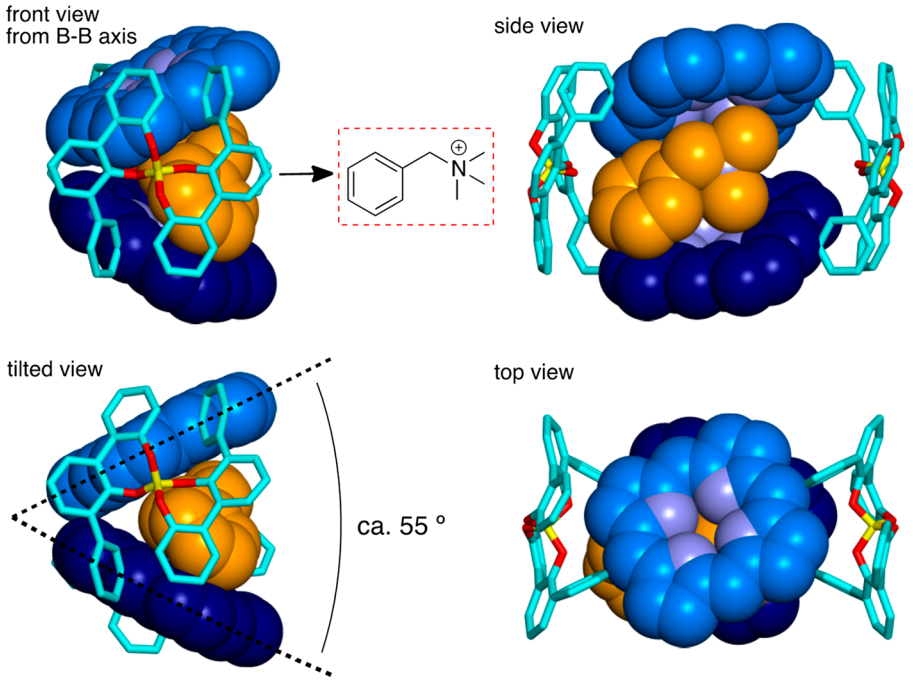

Figure 5. X-ray crystal structure of $\mathbf{1}_{BTMA2}$ ($\mathbf{1}_{BTMA}\supset$**BTMA**). All hydrogen atoms, ^{t}Bu groups, and another benzyltrimethylammonium (BTMA) molecule have been omitted for clarity. The porphyrin rings (light and dark blue) and the included BTMA molecule (orange) are highlighted as a space-filling model. The tilt angle between the two porphyrin rings is also shown.

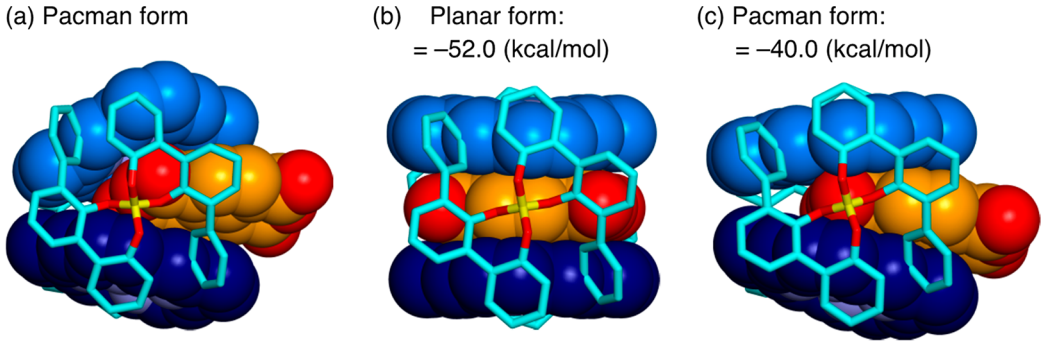

Figure 6. Snapshot of (a) the packman form of $\mathbf{1}^{2-}\supset$**G4** during the DFTB/US-MD simulation and the optimized geometries of the (b) planar and (c) packman forms of $\mathbf{1}^{2-}\supset$**G4**, which were calculated by RI-DFT. The binding energies (E_{bind}) of the optimized forms, which were calculated based on the binding energies of free helicate $\mathbf{1}^{2-}$ and **G4** as a base value (E_{bind} = 0), are also shown (panels b and c).

determined by X-ray crystallography with respect to the orientation of the two porphyrin rings (tilted or parallel).[6g]

We anticipated that the observed pacman-like structure of $\mathbf{1}_{BTMA}\supset$**BTMA** is one of the possible intermediates that is most likely relevant to the encapsulation mechanism of aromatic guests in the bisporphyrin helicate in nonaqueous media (Figure 1c, route A), which may be more plausible than another mechanism (Figure 1c, route B) by which the two porphyrin rings of the helicate are forced to expand in a parallel fashion so as to generate a sufficient space to sandwich an aromatic guest between the bisporphyrin. The latter parallel expansion mechanism may be thermodynamically unfavorable compared to the former pacman-type expansion of the two porphyrin rings, judging from the crystal structure of $\mathbf{1}_{Na2}$ in which the two porphyrin units are stacked face-to-face at a distance of 4.1 Å.[6g,18] Therefore, the two porphyrins linked in a face-to-face parallel arrangement favorably undergo the dynamic motion of unfolding while maintaining a partial overlap between the porphyrin rings to open a window for the guest uptake in such a way as to form the pacman-like inclusion complex, which subsequently folds into a face-to-face sandwich structure with the guest (Figure 1c, route A).

Theoretical Studies of the Mechanism of Guest Encapsulation in the Helicate. The complexation processes of $\mathbf{1}^{2-}\supset$**G4** and $\mathbf{1}_{(BTMA)2}\supset$**BTMA**$^+$ were then investigated by performing self-consistent charge density functional tight-binding (SCC-DFTB)[19] MD simulations with umbrella sampling (US) (DFTB/US-MD) using the crystal structures as the initial geometries (Figures S25 and S27) (see section 7 in the Supporting Information for theoretical background and computational details). During the DFTB/US-MD simulations of $\mathbf{1}^{2-}\supset$**G4**, we found both planar and pacman-like structures of $\mathbf{1}^{2-}\supset$**G4** in the trajectories (Figures 6a and S28a and b); such a pacman form was not observed in the corresponding crystal structures. We then optimized the geometries of the planar and pacman forms of the $\mathbf{1}^{2-}\supset$**G4** obtained by the DFTB/US-MD simulations using resolution of identity density functional theory (RI-DFT)[20] (Figure 6b and c) and

https://doi.org/10.1021/acs.joc.1c01155
J. Org. Chem. 2021, 86, 10501−10516

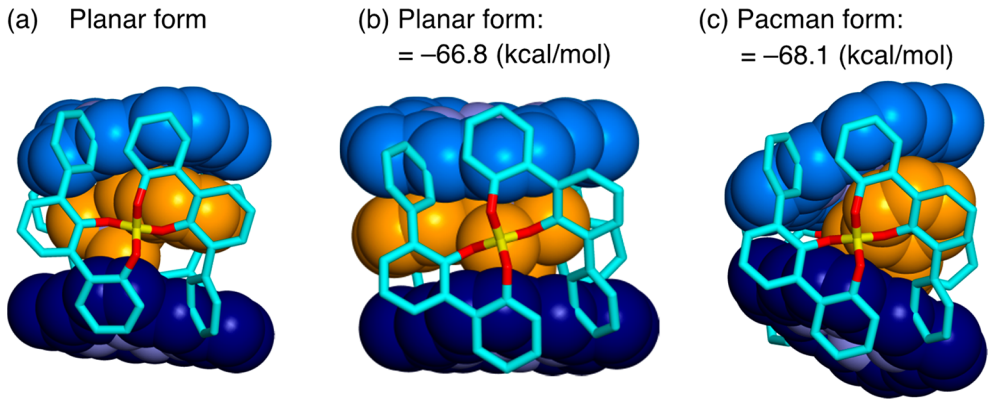

Figure 7. Snapshot of (a) the planar form of $\mathbf{1}_{(BTMA)_2}\supset\mathbf{BTMA}^+$ during the DFTB/US-MD simulation and the optimized geometries of the (b) planar and (c) packman forms of $\mathbf{1}_{(BTMA)_2}\supset\mathbf{BTMA}^+$, which were calculated by RI-DFT. The binding energies (E_{bind}) of the optimized forms, which were calculated based on the binding energies of free helicate $\mathbf{1}_{(BTMA)_2}$ and $\mathbf{BTMA}^+$ as a base value (E_{bind} = 0), are also shown (panels b and c).

computed binding energy (E_{bind}) values. The planar and pacman forms were maintained during the optimization, indicating that both forms are local-minimum free-energy states; the two porphyrin rings are tilted by 21.5° in the pacman form and by 1.2° in the planar form, respectively. The E_{bind} value of the planar geometry was lower than that of the pacman-like geometry by 12 kcal mol^{-1} (Figure 6b and c).

We also calculated the potential of mean force (PMF) $F_{T_0}(\xi)$, which is the Helmholtz free energy as a function of the reaction coordinate ξ in the original unbiased system, using the DFTB/US-MD simulation as shown in Figure S29. The PMF shows that the planar form at around $\xi(r)$ = 0.0 Å is more stable than the pacman form at around $\xi(r)$ = 4.0 Å, corresponding to the E_{bind} value. The PMF also shows that the free-energy barrier from the planar form to the pacman form is less than 1.0 kcal mol^{-1} (Figure S29). According to the computational results, we found one case where the pacman form is one of the intermediate states, which immediately transformed into the planar form by overcoming a low free-energy barrier. This might be the reason why only the planar $\mathbf{1}^{2-}\supset\mathbf{G4}$ has been found by X-ray analysis. This mechanism suggests that it should be difficult to capture the pacman form in experiments.

In the same way, we performed the DFTB/US-MD simulations and geometry optimizations of $\mathbf{1}_{(BTMA)_2}\supset\mathbf{BTMA}^{+}$[21] by RI-DFT and computed both the E_{bind} values (Figure 7) and the PMF (Figure S30). The optimized planar and pacman forms obtained from the DFTB/US-MD simulations are shown in Figure 7b and c, respectively. Although the planar form has not been obtained by the X-ray analysis (Figure 5), the optimized geometries still maintained both the planar and pacman forms. The E_{bind} value of the pacman form was lower than that of the planar one by 1.3 kcal mol^{-1} (Figure 7b and c), indicating that the pacman form of $\mathbf{1}_{(BTMA)_2}\supset\mathbf{BTMA}^+$ is more stable than the planar one. In the PMF of $\mathbf{1}_{(BTMA)_2}\supset\mathbf{BTMA}^+$ (Figure S30), the pacman form located at around $\xi(r)$ = 2.2 Å is more stable than the planar form located at around $\xi(r)$ = 0.0 Å. This is consistent with the tendency of E_{bind}, and it seems that the planar form tends to transform into the pacman form because of the lower free-energy of the pacman form. Therefore, this energetic relationship points to the likely reason why only the pacman form of $\mathbf{1}_{BTMA}\supset\mathbf{BTMA}$ was observed by X-ray analysis.

Kinetic Studies of the Inclusion and Release of Aromatic Guests into and from the Helicate. The ^{1}H NMR spectra of mixtures of $\mathbf{1}_{Na2}$ with 0.5 equiv of the NMI (**G10**–**G12**) and NDI (**G13**–**G15**) derivatives derived from **G4** also displayed two sets of signals due to the presence of free $\mathbf{1}_{Na2}$ and the corresponding 1:1 inclusion complexes as already described for **G4** and the PDI derivative **G6** (Figures S7 and S9, respectively), which were almost independent of their K_a values (Figures S12–S17, respectively, and Table 1).[22] Similar but rather broad signals appeared when $\mathbf{1}_{Na2}$ was mixed with 0.5 equiv of **G1** and **G3** (Figures S4c and S6c, respectively), indicating that the exchanges between the free $\mathbf{1}_{Na2}$ and its complexes with **G1** and **G3** were faster than that with **G4**. Although the K_a value of $\mathbf{1}_{Na2}$ with **G2** was similar to those with **G1**, **G3**, **G14**, and **G15** and approximately five-times greater than that with **G13** (Table 1), the exchange between the free $\mathbf{1}_{Na2}$ and its complex with **G2** was much faster than those with **G1**, **G3**, **G4**, **G6**, and **G10**–**G15**. Therefore, the mixing of $\mathbf{1}_{Na2}$ with 0.5 equiv of **G2** showed broad ^{1}H NMR signals that were averaged between the free $\mathbf{1}_{Na2}$ and its inclusion complex with **G2**, and the ^{1}H signals of **G2** complexed with $\mathbf{1}_{Na2}$ could not be observed (Figure S5).

The kinetics of the guest inclusion and release into and from $\mathbf{1}_{Na2}$ were further investigated by the 2D EXSY measurements of 1:1 mixtures of $\mathbf{1}_{Na2}$ and its inclusion complexes with selected guests, $\mathbf{1}_{Na2}\supset\mathbf{GX}$ (**X** = **4**, **14**, and **15**). Each 1:1 mixture was generated upon the addition of 0.5 equiv of the guest to a solution of $\mathbf{1}_{Na2}$ in CD_3CN at 30 °C, which displayed a number of chemical exchange cross-peaks between the free $\mathbf{1}_{Na2}$ and $\mathbf{1}_{Na2}\supset\mathbf{GX}$ (**X** = **4**, **14**, and **15**) (Figures S31–S33, respectively). By measuring the peak volumes of the cross and diagonal peaks at different mixing times, the apparent exchange rate constants (k_{ex}) between the free $\mathbf{1}_{Na2}$ and its inclusion complexes with **GX** (**X** = **4**, **14**, and **15**) were estimated to be 0.023, 4.3, and 0.40 s^{-1}, respectively. The results revealed that the inclusion and release process of the nonsubstituted **G4** toward $\mathbf{1}_{Na2}$ was extremely slow, as was anticipated from its very high binding affinity (K_a = ca. 2.2 × 10^9 M^{-1}) compared to those of the NDI-based guests **14** (ca. 5.2 × 10^5 M^{-1}) and **15** (ca. 2.0 × 10^5 M^{-1}) derived from **G4** (Table 1). On the other hand, the exchange rate for **G15** bearing the benzyl substituents is approximately 10× slower than that for **G14** bearing less bulky *n*-butyl substituents but approximately 17× faster than that for **G4**. These 2D EXSY and 1D NMR results suggested that the guest inclusion and release process into and from $\mathbf{1}_{Na2}$ is highly dependent on the presence or absence of the substituents of the guests as well as

https://doi.org/10.1021/acs.joc.1c01155
J. Org. Chem. 2021, 86, 10501–10516

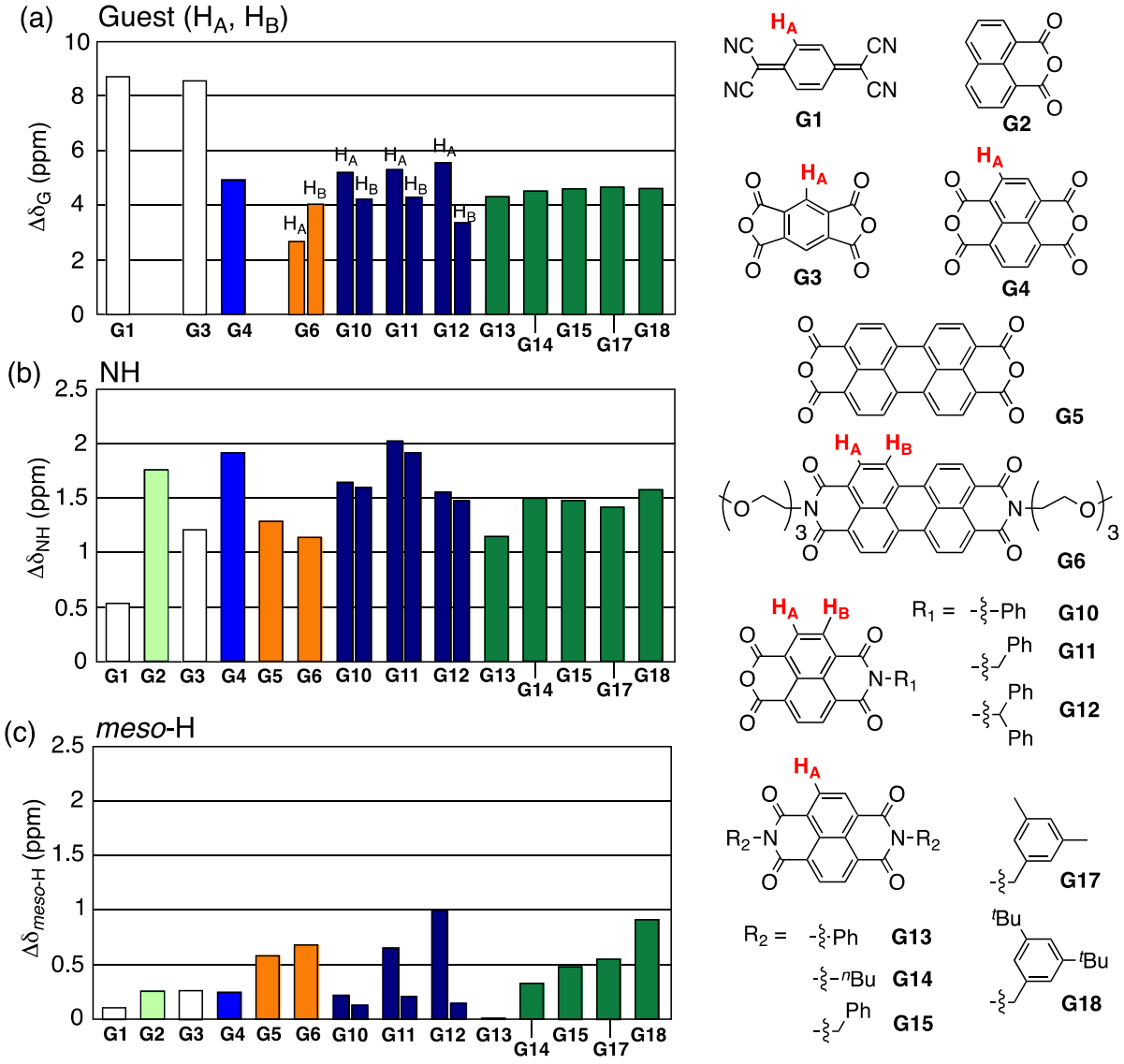

Figure 8. Summary of the complexation-induced ^{1}H chemical shift changes of (a) the aromatic protons of guests ($\Delta\delta_G$), (b) those of the pyrrole NH ($\Delta\delta_{NH}$), and (c) the *meso*-H protons ($\Delta\delta_{meso\text{-}H}$) of $\mathbf{1}_{Na2}$.

the type of substituents (aliphatic or aromatic), which likely contributes to the strength of the π-stacking interaction between the aromatic core of the guests and the bisporphyrin unit of the helicate.

Encapsulated Guest Structures within the Helicate. The encapsulation of electron-deficient aromatic guests between the bisporphyrin causes significant changes in the chemical shifts of the aromatic protons of the guests ($\Delta\delta_G$)[23] along with the specific porphyrin proton signals of $\mathbf{1}_{Na2}$, such as the pyrrole NH ($\Delta\delta_{NH}$) and *meso*-H protons ($\Delta\delta_{meso\text{-}H}$) (see Figure 1a), due to the porphyrin ring current effect and the shielding effect of the included aromatic rings of the guests, respectively. These changes provide useful information regarding the structures of the encapsulated guests, such as the orientations relative to the two porphyrin rings of $\mathbf{1}_{Na2}$.[24] The complexation-induced chemical shift changes ($\Delta\delta_G$, $\Delta\delta_{NH}$, and $\Delta\delta_{meso\text{-}H}$) of $\mathbf{1}_{Na2}$ with 0−5 equiv of **GX** (**X** = **1**−**6**, **10**−**15**, **17**, and **18**) were then investigated in CD_3CN at 25 °C (Figures S4 − S21), and the results are summarized in Table 1 and Figure 8.

The H_A or H_B proton NMR signals for all of the tested electron-deficient aromatic guests were significantly shifted upfield upon the formation of a 1:1 sandwich complex with $\mathbf{1}_{Na2}$. A more pronounced upfield shift of the H_A signals was observed for **G1** and **G3**, which were composed of a smaller phenylene core ($\Delta\delta_G$ = 8.71 and 8.56 ppm, respectively), indicating that the protons of smaller aromatic guests (**G1** and **G3**) are located at the center of the bisporphyrin. Therefore, the $\Delta\delta_G$ values of the guests tended to decrease in the following order: **G1** and **G3** > **G4**, **G10**−**G15**, **G17**, and **G18** > **G6**, which is in good agreement with the order of the aromatic core size (Figure 8a).

As anticipated, the guest-induced chemical shift changes of the inner pyrrole NH protons of the porphyrin rings of $\mathbf{1}_{Na2}$ ($\Delta\delta_{NH}$) were always greater than those of the *meso*-H protons on the periphery of the porphyrin rings ($\Delta\delta_{meso\text{-}H}$) independent of the guest structures as a result of the π-stacked geometry and showed roughly similar values except for the guests with small (**G1** and **G3**) and large cores (**G5** and **G6**) (Figure 8b). The $\Delta\delta_{meso\text{-}H}$ values are highly affected by the guests, namely, their core sizes and substituents (Figure 8c). **G1** exerted little

https://doi.org/10.1021/acs.joc.1c01155
J. Org. Chem. 2021, 86, 10501−10516

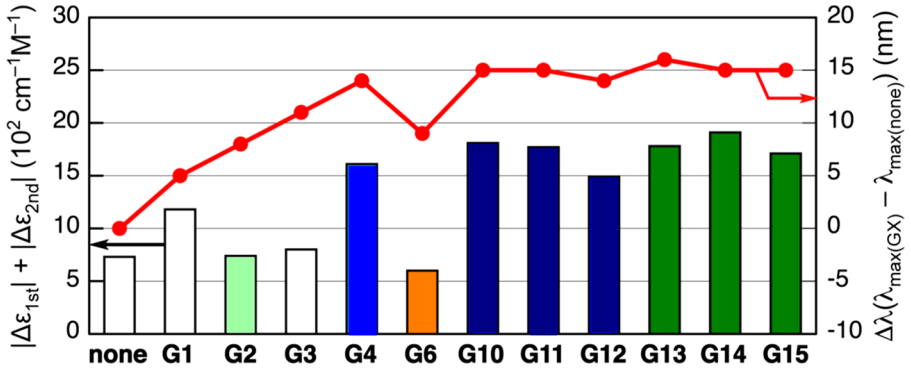

Figure 9. Summary of the complexation-induced CD intensity ($|\Delta\varepsilon_{first}| + |\Delta\varepsilon_{second}|$) and absorption maximum ($\Delta\lambda$) changes of (*M*)-$\mathbf{1}_{TBA2}$.

influence compared to **G2**−**G4**, while **G5** and **G6**, which were composed of large perylene cores, induced a greater upfield shift of the *meso*-H protons.

When complexed with nonsymmetric NMI-based guests (**G11** and **G12**) (Figures S13 and S14), one of the *meso*-H protons was shifted more upfield than the other *meso*-H proton of the porphyrin rings on the opposite side due to the aromatic shielding effects of the *N*-benzyl and *N*-diphenylmethyl groups of the pendants. Hence, relatively high $\Delta\delta_{meso\text{-}H}$ values (0.48−0.91) were observed for the NDI-based guests **G15**, **G17**, and **G18** bearing *N*-benzyl and bulky *N*-3,5-dimethy- and 3,5-di-*tert*-butylbenzyl substituents on both sides, respectively (Figures 8c, S17, S19, and S20, respectively, and Table 1). Interestingly, the *N*-benzyl methylene proton signals of the NDI-based achiral guests (**G15**, **G17**, and **G18**) complexed with $\mathbf{1}_{Na2}$ were shifted upfield and split into a pair of doublets with relatively large chemical shift differences ($\Delta\delta_{CH2}$) of 0.23, 0.32, and 0.16 ppm, respectively (Figures 2h,i, S17, S19, and S20), indicating that the *N*-benzyl methylene groups were magnetically nonequivalent once encapsulated in the double-stranded helical $\mathbf{1}_{Na2}$. The helical chirality of $\mathbf{1}_{Na2}$ appears to force the guests to bind in a diastereotopic environment, thereby allowing the recognition of the enantiotopic methylene groups.[2S] Therefore, the enantiopure left-handed double-helical (*M*)-$\mathbf{1}_{TBA2}$ can discriminate between the enantiomers of NMI-based racemic guests bearing a chiral aromatic substituent at one end and can form an inclusion complex with one of the enantiomers in a highly diastereoselective fashion, as detected by ^{1}H NMR.[6i]

The enantiopure (*M*)-$\mathbf{1}_{TBA2}$ helicate showed a bisignated exciton-coupled Cotton effect in the porphyrin Soret band region due to the two porphyrin rings being twisted into a right-handed orientation.[6g] Upon the encapsulation of an electron-deficient aromatic guest, such as **G4**, the exciton-coupled circular dichroism (CD) spectral pattern and the intensity of (*M*)-$\mathbf{1}_{TBA2}$ were drastically changed and enhanced, respectively. This was accompanied by a large red-shift of its absorption maximum (λ_{max}), which resulted from the expansion of the bisporphyrin cavity and the subsequent rotary motion of the porphyrin rings in one direction coupled with a unidirectional twisting motion of the spiroborate helix.[6g] We anticipated that these unidirectional dual rotary and twisting motions of the helicate could be changed by guests composed of different-sized aromatic cores. We then measured the CD spectra of (*M*)-$\mathbf{1}_{TBA2}$ complexed with a series of guests (Figures S34−S36), and the results are summarized in Figure 9 and Table S6.

The CD spectral patterns and intensities and the λ_{max} values of (*M*)-$\mathbf{1}_{TBA2}$ complexed with **G4** and the NMI- (**G10**−**G12**) and NDI-based guests (**G13**−**G15**) were almost similar to each other, showing enhanced Cotton effects independent of the structures and the number of substituents of the guests composed of a naphthalene core (Figure 9). In contrast, the inclusion complexes of (*M*)-$\mathbf{1}_{TBA2}$ with smaller and less electron-deficient aromatic guests (**G2** and **G3**) showed almost no enhancement of the CD, while that with **G1** induced a slightly intense split-type CD; all were accompanied by a gradual red-shift of the λ_{max} in the following order: **G1** < **G2** < **G3** < (**G4**, **G10**−**G15**) (Figure 9). On the other hand, a PDI-based guest **G6** with a large perylene core also displayed almost no enhancement of the CD intensity, but its bisignated CD at higher wavelengths and spectral pattern were different from those of the other inclusion complexes, mostly due to the exciton coupling between the bisporphyrin and PDI chromophores (Figures 9 and S34).

These results suggested that the guest-encapsulation-induced CD spectral changes of (*M*)-$\mathbf{1}_{TBA2}$ and with their ^{1}H NMR spectral changes ($\Delta\delta$ values) (Figures 8 and 9) may provide useful information about the spatial arrangement or alignment of the guests sandwiched between the bisporphyrin unit, which may be responsible for the dual rotary and twisting motions of the helicate.

■ CONCLUSIONS

In this study, we systematically investigated the formation of an inclusion complex between the porphyrin-linked double-stranded spiroborate helicate and a series of electron-deficient aromatic guests. We have found that the thermodynamic and kinetic stabilities of the inclusion complexes are highly dependent on the core sizes of the aromatic guests as well as the bulkiness and number of substituents of the guests. Although naphthalenediimide-based guests with bulky substituents at both ends could not pass through the bisporphyrin cavity, a small amount of water promoted the dynamic B−O bond cleavage/reformation of the spiroborate groups of the helicate, resulting in the formation of a [2]rotaxane-like inclusion complex. The unique pacman-like 1:1 inclusion complex revealed by an X-ray crystal structure analysis and further supported by MD simulations suggests that a pacman-like structure may be more plausible as an intermediate for the inclusion of a planar aromatic guest within the bisporphyrin cavity of the helicate. Taking advantage of both the right- and left-handed porphyrin-linked spiroborate helicates that are readily available,[6g] the present results will provide a promising way to control the rotary and twisting motions of the helicate

https://doi.org/10.1021/acs.joc.1c01155
J. Org. Chem. 2021, 86, 10501−10516

in one direction in a more precise manner that can be triggered by the inclusion of specific chiral aromatic guests within the bisporphyrin chiral cavity, which may be further applicable to the development of unique supramolecular asymmetric catalysts. Its catalytic activity and enantioselectivity will be regulated by the guest-induced unidirectional rotary and twisting motions of the helicate.

EXPERIMENTAL SECTION

General Information. The NMR spectra were recorded using a Bruker Ascend 500 (Bruker Biospin, Billerica, MA) or a Varian 500AS (Varian, Palo Alto, CA) spectrometer operating at 500 MHz for ^{1}H and 125 MHz for ^{13}C, using tetramethylsilane (TMS) or a residual undeuterated solvent peak as the internal standard. The absorption and CD spectra were measured in a 0.1 or 1 cm quartz cell using a JASCO V-570 spectrophotometer and a JASCO J-820 or a J-1500 spectropolarimeter, respectively. The fluorescence spectra were recorded in a 1 cm quartz cell on a JASCO FP-6500 spectrofluorometer. The SEC fractionations were performed using an LC-908W−C60 liquid chromatograph (Japan Analytical Industry) equipped with two SEC columns (JAIGEL-1H-40 (4 (i.d.) × 60 cm) and JAIGEL-2H-40 (4 (i.d.) × 60 cm)) in series and UV−visible (JAI UV-3702) and RI (JAI RI-5) detectors; chloroform ($CHCl_3$) was used as the eluent at a flow rate of 12 mL min^{-1}. All starting materials, including aromatic guests (**G1**−**G5** and **G7**−**G9**), were purchased from commercial suppliers and used without further purification unless otherwise noted. The spiroborate helicate $\mathbf{1}_{Na2}$ and its enantiomer complexed with an achiral tetra-*n*-butylammonium (TBA) cation, (*M*)-$\mathbf{1}_{TBA2}$,[6g] **G6**,[26] **G13**,[27] **G14**,[28] 3,5-dimethylbenzylamine,[29] and 3,5-di-*tert*-butylbenzylamine,[29] were prepared according to the literature.

Synthesis of Naphthalene-Based Guests. ***G10***. To a solution of **G4** (300 mg, 1.11 mmol) in DMF (20 mL) was added aniline (0.10 mL, 1.1 mmol) at 90 °C under argon in an oil bath, and the reaction mixture was stirred at 150 °C for 30 min in an oil bath. After cooling to ambient temperature, the solvent was removed under reduced pressure. The resulting brown residue was then suspended in acetone, and to the mixture was slowly added H_2O with vigorous stirring. The precipitate was dissolved in $CHCl_3$, and the solution was dried over anhydrous Na_2SO_4, filtered, and concentrated under reduced pressure. The crude product was purified by SEC ($CHCl_3$ as the eluent), affording **G10** as a white solid (109 mg, 28% yield). mp: 321 °C (decomp.). IR (KBr, cm^{-1}): 1781 ($\nu_{C=O}$), 1750 ($\nu_{C=O}$), 1719 ($\nu_{C=O}$), 1681 ($\nu_{C=O}$). ^{1}H NMR (500 MHz, $CDCl_3$, 25 °C): δ 8.88 (d, 2H, J = 7.5 Hz), 8.86 (d, J = 7.5 Hz, 2H), 7.60 (br dd, 2H), 7.55 (br tt, 1H), 7.33 (br dd, 2H). ^{13}C{^{1}H} NMR (125 MHz, $CDCl_3$, 25 °C): δ 162.5, 158.9, 134.4, 133.4, 131. 8, 129.8, 129.6, 129.2, 128.5, 128.2, 127.4, 123.3. Anal. Calcd for $C_{20}H_9NO_5$: C, 69.98; H, 2.64; N, 4.08. Found: C, 69.99; H, 2.58; N, 4.06.

G11 and G15. To a solution of **G4** (300 mg, 1.11 mmol) in DMF (3.0 mL) was added benzylamine (0.12 mL, 1.1 mmol) at 140 °C under argon in an oil bath, and the reaction mixture was stirred at 170 °C for 30 min in an oil bath. After cooling to ambient temperature, the solvent was removed under reduced pressure. The resulting brown residue was then suspended in acetone, and to the mixture was slowly added 1 M aqueous HCl with vigorous stirring. The precipitate was dissolved in $CHCl_3$, and the solution was dried over anhydrous Na_2SO_4, filtered, and concentrated under reduced pressure. The crude product contained a mixture of **G11** and **G15**, which was separated by SEC ($CHCl_3$ as the eluent) into **G11** (93.9 mg, 24% yield) and **G15** (111 mg, 22% yield) as white solids.

G11. mp: 279.1−280.9 °C. IR (KBr, cm^{-1}): 1785 ($\nu_{C=O}$), 1742 ($\nu_{C=O}$), 1710 ($\nu_{C=O}$), 1671 ($\nu_{C=O}$). ^{1}H NMR (500 MHz, $CDCl_3$, 25 °C): δ 8.84 (d, 2H, J = 8.0 Hz), 8.81 (d, J = 7.5 Hz, 2H), 7.55 (br dd, 2H), 7.33 (br dd, 2H), 7.28 (br tt, 1H), 5.40 (s, 2H). ^{13}C{^{1}H} NMR (125 MHz, $CDCl_3$, 25 °C): δ 162.4, 158.9, 136.4, 133.3, 131.6, 129.4, 129.0, 128.8, 128.2, 128.0, 127.0, 123.1, 44.4. Anal. Calcd for $C_{21}H_{11}NO_5$: C, 70.59; H, 3.10; N, 3.92. Found: C, 70.60; H, 3.12; N, 3.96.

G15. mp: 271.8 °C (decomp.). IR (KBr, cm^{-1}): 1703 ($\nu_{C=O}$), 1665 ($\nu_{C=O}$). ^{1}H NMR (500 MHz, $CDCl_3$, 25 °C): δ 8.77 (s, 4H), 7.56 (br dd, 4H), 7.32 (br dd, 4H), 7.35 (br tt, 2H), 7.26 (m, 2H), 5.39 (s, 4H). ^{13}C{^{1}H} NMR (125 MHz, $CDCl_3$, 25 °C): δ 163.0, 136.7, 131.3, 129.3, 128.7, 128.0, 126.9, 126.8, 44.2. HRMS (ESI-TOF) m/z: [M − H]$^-$ Calcd for $C_{28}H_{18}N_2O_4$ 446.1267, found 446.1275.

G12 and G16. To a solution of **G4** (300 mg, 1.11 mmol) in DMF (3.0 mL) was added 1,1-diphenylmethylamine (0.19 mL, 1.1 mmol) at 160 °C under argon in an oil bath, and the reaction mixture was stirred at 160 °C for 30 min in an oil bath. After cooling to ambient temperature, the solvent was removed under reduced pressure. The resulting brown residue was then suspended in acetone, and to the mixture was slowly added 1 M aqueous HCl with vigorous stirring. The precipitate was dissolved in $CHCl_3$, and the solution was dried over anhydrous Na_2SO_4, filtered, and concentrated under reduced pressure. The crude product contained a mixture of **G12** and **G16**, which was separated by SEC ($CHCl_3$ as the eluent) into **G12** (136 mg, 28% yield) and **G16** (57.3 mg, 8.6% yield) as white and pale yellow solids, respectively.

G12. mp: 315 °C (decomp.). IR (KBr, cm^{-1}): 1782 ($\nu_{C=O}$), 1745 ($\nu_{C=O}$), 1712 ($\nu_{C=O}$), 1674 ($\nu_{C=O}$). ^{1}H NMR (500 MHz, $CDCl_3$, 25 °C): δ 8.80 (m, 4H), 7.63 (s, 1H), 7.45 (br dd, 4H), 7.36 (br dd, 4H), 7.32 (br tt, 2H). ^{13}C{^{1}H} NMR (125 MHz, $CDCl_3$, 25 °C): δ 162.4, 158.9, 137.9, 133.3, 131.8, 129.0, 128.9, 128.6, 128.2, 127.9, 127.1, 123.0, 60.1. Anal. Calcd for $C_{27}H_{15}NO_5$: C, 74.82; H, 3.49; N, 3.23. Found: C, 74.82; H, 3.53; N, 3.25.

G16. mp: 321 °C (decomp.). IR (KBr, cm^{-1}): 1709 ($\nu_{C=O}$), 1671 ($\nu_{C=O}$). ^{1}H NMR (500 MHz, $CDCl_3$, 25 °C): δ 8.72 (s, 4H), 7.63 (s, 2H), 7.45 (br dd, 8H), 7.35 (br dd, 8H), 7.30 (br tt, 4H). ^{13}C{^{1}H} NMR (125 MHz, $CDCl_3$, 25 °C): δ 162.9, 138.0, 131.5, 128.8, 128.4, 127.60, 126.9, 126.8, 59.6. HRMS (ESI-TOF) m/z: [M − H]$^-$ Calcd for $C_{40}H_{26}N_2O_4$ 598.1893, found 598.1877.

G17. To a solution of **G4** (200 mg, 0.746 mmol) in DMF (3.0 mL) was added 3,5-dimethylbenzylamine (0.33 mL, 2.3 mmol) at ambient temperature under argon, and the reaction mixture was stirred at 140 °C for 30 min in an oil bath. After cooling to ambient temperature, the solvent was removed under reduced pressure. The resulting brown residue was washed with Et_2O and dried under vacuum to afford **G17** (319 mg, 85% yield) as a yellow solid. mp: 384 °C (decomp.). IR (KBr, cm^{-1}): 1706 ($\nu_{C=O}$), 1666 ($\nu_{C=O}$). ^{1}H NMR (500 MHz, $CDCl_3$, 25 °C): δ 8.77 (s, 4H), 7.14 (s, 4H), 6.90 (s, 2H), 5.32 (s, 4H), 2.28 (s, 12H). ^{13}C{^{1}H} NMR (125 MHz, $CDCl_3$, 25 °C): δ 163.0, 138.3, 136.5, 131.3, 129.7, 126.91, 126.87, 126.8, 44.1, 21.4. HRMS (ESI-TOF) m/z: [M − H]$^-$ Calcd for $C_{32}H_{26}N_2O_4$ 502.1893, found 502.1899.

G18. To a solution of **G4** (200 mg, 0.746 mmol) in DMF (3.0 mL) was added 3,5-di-*tert*-butylbenzylamine (0.33 mL, 2.3 mmol) at ambient temperature under argon. The reaction mixture was stirred at 150 °C for 30 min in an oil bath and further at 100 °C for 11 h in an oil bath. After cooling to ambient temperature, the solution was poured into a large amount of Et_2O. The resulting precipitate was filtered, washed with Et_2O, and dried under vacuum to afford **G18** (449 mg, 85% yield) as a white solid. mp: 318.9−320.8 °C. IR (KBr, cm^{-1}): 1708 ($\nu_{C=O}$), 1666 ($\nu_{C=O}$). ^{1}H NMR (500 MHz, $CDCl_3$, 25 °C): δ 8.75 (s, 4H), 7.47 (d, J = 1.9 Hz, 4H), 7.35 (dd, J = 1.9 Hz, 2H), 5.37 (s, 4H), 1.30 (s, 36H). ^{13}C{^{1}H} NMR (125 MHz, $CDCl_3$, 25 °C): δ 163.0, 151.1, 135.9, 131.2, 126.9, 126.8, 124.2, 122.1, 44.6, 35.0, 31.6. HRMS (ESI-TOF) m/z: [M − H]$^-$ Calcd for $C_{44}H_{50}N_2O_4$ 670.3771, found 670.3775.

G19. To a solution of **G4** (200 mg, 0.746 mmol) in DMF (10 mL) was added 1-adamantanemethylamine (0.31 mL, 1.9 mmol) at ambient temperature under argon, and the reaction mixture was stirred at 140 °C for 30 min in an oil bath. After cooling to ambient temperature, the solution was poured into a large amount of Et_2O. The resulting precipitate was filtered, washed with Et_2O, and dried under vacuum to afford **G19** (328 mg, 78% yield) as a pale pink solid. mp: 365 °C (decomp.). IR (KBr, cm^{-1}): 1708 ($\nu_{C=O}$), 1671 ($\nu_{C=O}$). ^{1}H NMR (500 MHz, $CDCl_3$, 25 °C): δ 8.76 (s, 4H), 4.05 (s, 4H), 1.96 (s, 6H), 1.59−1.69 (m, 24H). ^{13}C{^{1}H} NMR (125 MHz,

https://doi.org/10.1021/acs.joc.1c01155
J. Org. Chem. 2021, 86, 10501−10516

$CDCl_3$, 25 °C): δ 163.9, 131.3, 126.82, 126.81, 51.1, 41.5, 36.9, 36.2, 28. 6. Anal. Calcd for $C_{36}H_{38}N_2O_4$: C, 76.84; H, 6.81; N, 4.98. Found: C, 76.85; H, 6.80; N, 5.00.

■ ASSOCIATED CONTENT

Supporting Information

The Supporting Information is available free of charge at https://pubs.acs.org/doi/10.1021/acs.joc.1c01155.

Full experimental details, characterizations of inclusion complexes, modeling procedures, and additional supporting data (PDF)

Accession Codes

CCDC 1559425 contains the supplementary crystallographic data for this paper. These data can be obtained free of charge via www.ccdc.cam.ac.uk/data_request/cif, or by emailing data_request@ccdc.cam.ac.uk, or by contacting The Cambridge Crystallographic Data Centre, 12 Union Road, Cambridge CB2 1EZ, UK; fax: +44 1223 336033.

■ AUTHOR INFORMATION

Corresponding Authors

Naoki Ousaka − *Department of Molecular Design and Engineering, Graduate School of Engineering and Department of Molecular and Macromolecular Chemistry, Graduate School of Engineering, Nagoya University, Nagoya 464-8603, Japan;* Present Address: N.O.: Molecular Engineering Institute, Kyushu Institute of Technology, Tobata-ku, Kitakyushu 804-8550, Japan; orcid.org/0000-0002-3398-3328; Email: ousaka.naoki@gmail.com

Yuh Hijikata − *Department of Chemistry, Graduate School of Science, Nagoya University, Nagoya 464-8602, Japan; Institute of Transformative Bio-Molecules (WPI-ITbM), Nagoya University, Nagoya 464-8601, Japan;* Present Address: Y.H.: Institute for Chemical Reaction Design and Discovery (WPI-ICReDD), Hokkaido University, Sapporo, 001-0021, Japan.; orcid.org/0000-0003-4883-5085; Email: hijikata@icredd.hokudai.ac.jp

Eiji Yashima − *Department of Molecular Design and Engineering, Graduate School of Engineering and Department of Molecular and Macromolecular Chemistry, Graduate School of Engineering, Nagoya University, Nagoya 464-8603, Japan;* orcid.org/0000-0001-6307-198X; Email: yashima@chembio.nagoya-u.ac.jp

Authors

Shinya Yamamoto − *Department of Molecular Design and Engineering, Graduate School of Engineering, Nagoya University, Nagoya 464-8603, Japan*

Hiroki Iida − *Department of Molecular Design and Engineering, Graduate School of Engineering, Nagoya University, Nagoya 464-8603, Japan;* Present Address: H.I.: Department of Chemistry, Graduate School of Natural Science and Technology, Shimane University, 1060 Nishikawatsu, Matsue 690-8504, Japan.; orcid.org/0000-0002-7114-0364

Takuya Iwata − *Department of Molecular Design and Engineering, Graduate School of Engineering, Nagoya University, Nagoya 464-8603, Japan*

Shingo Ito − *Department of Chemistry, Graduate School of Science, Nagoya University, Nagoya 464-8602, Japan;* Present Address: S.I.: Theoretical Molecular Science Laboratory, RIKEN Cluster for Pioneering Research, Wako, Saitama, 351-0198, Japan.

Rafael Souza − *Department of Chemistry, Graduate School of Science, Nagoya University, Nagoya 464-8602, Japan*

Stephan Irle − *Department of Chemistry, Graduate School of Science, Nagoya University, Nagoya 464-8602, Japan; Institute of Transformative Bio-Molecules (WPI-ITbM), Nagoya University, Nagoya 464-8601, Japan;* Present Address: S.I.: Computational Sciences & Engineering Division, Oak Ridge National Laboratory, Oak Ridge, Tennessee 37831-6129, USA.; orcid.org/0000-0003-4995-4991

Complete contact information is available at: https://pubs.acs.org/10.1021/acs.joc.1c01155

Notes

The authors declare no competing financial interest.

■ ACKNOWLEDGMENTS

This work was supported in part by JSPS KAKENHI (Grant-in-Aid for Specially Promoted Research, no. 18H05209 (E.Y.)). We thank Dr. Daisuke Taura (Nagoya University) for his help in the modeling of the helicates.

■ REFERENCES

(1) (a) Dietrich, B.; Lehn, J. M.; Sauvage, J. P. Les Cryptates. *Tetrahedron Lett.* **1969**, *10*, 2889−2892. (b) Moran, J. R.; Karbach, S.; Cram, D. J. Cavitands: Synthetic Molecular Vessels. *J. Am. Chem. Soc.* **1982**, *104*, 5826−5828.

(2) Reviews: (a) Anslyn, E. V. Supramolecular Analytical Chemistry. *J. Org. Chem.* **2007**, *72*, 687−699. (b) Yoshizawa, M.; Klosterman, J. K.; Fujita, M. Functional Molecular Flasks: New Properties and Reactions within Discrete, Self-Assembled Hosts. *Angew. Chem., Int. Ed.* **2009**, *48*, 3418−3438. (c) Gale, P. A. From Anion Receptors to Transporters. *Acc. Chem. Res.* **2011**, *44*, 216−226. (d) Ogoshi, T.; Yamagishi, T. Pillararenes: Versatile Synthetic Receptors for Supramolecular Chemistry. *Eur. J. Org. Chem.* **2013**, *2013*, 2961−2975. (e) Wu, X.; Li, Z.; Chen, X. X.; Fossey, J. S.; James, T. D.; Jiang, Y. B. Selective Sensing of Saccharides Using Simple Boronic Acids and Their Aggregates. *Chem. Soc. Rev.* **2013**, *42*, 8032−8048. (f) Raynal, M.; Ballester, P.; Vidal-Ferran, A.; van Leeuwen, P. W. N. M. Supramolecular Catalysis. Part 1: Non-Covalent Interactions as a Tool for Building and Modifying Homogeneous Catalysts. *Chem. Soc. Rev.* **2014**, *43*, 1660−1733. (g) Brown, C. J.; Toste, F. D.; Bergman, R. G.; Raymond, K. N. Supramolecular Catalysis in Metal−Ligand Cluster Hosts. *Chem. Rev.* **2015**, *115*, 3012−3035. (h) Barboiu, M. Encapsulation versus Self-Aggregation toward Highly Selective Artificial K^+ Channels. *Acc. Chem. Res.* **2018**, *51*, 2711−2718. (i) Guo, C.; Sedgwick, A. C.; Hirao, T.; Sessler, J. L. Supramolecular Fluorescent Sensors: An Historical Overview and Update. *Coord. Chem. Rev.* **2021**, *427*, 213560.

(3) For reviews of the bisporphyrin-based receptors, see: (a) Tashiro, K.; Aida, T. Metalloporphyrin Hosts for Supramolecular Chemistry of Fullerenes. *Chem. Soc. Rev.* **2007**, *36*, 189−197. (b) Berova, N.; Pescitelli, G.; Petrovic, A. G.; Proni, G. Probing Molecular Chirality by CD-Sensitive Dimeric Metalloporphyrin Hosts. *Chem. Commun.* **2009**, 5958−5980. (c) Borovkov, V. Supramolecular Chirality in Porphyrin Chemistry. *Symmetry* **2014**, *6*, 256−294. (d) Durola, F.; Heitz, V.; Reviriego, F.; Roche, C.; Sauvage, J. P.; Sour, A.; Trolez, Y. Cyclic [4]Rotaxanes Containing Two Parallel Porphyrinic Plates: Toward Switchable Molecular Receptors and Compressors. *Acc. Chem. Res.* **2014**, *47*, 633−645. (e) Durot, S.; Taesch, J.; Heitz, V. Multiporphyrinic Cages: Architectures and Functions. *Chem. Rev.* **2014**, *114*, 8542−8578. (f) Valderrey, V.; Aragay, G.; Ballester, P. Porphyrin Tweezer Receptors: Binding Studies, Conformational Properties and Applications. *Coord. Chem. Rev.* **2014**, *258−259*, 137−156. (g) Lu, H.; Kobayashi, N. Optically Active Porphyrin and Phthalocyanine Systems. *Chem. Rev.* **2016**, *116*, 6184−6261.

(h) Mondal, P.; Rath, S. P. Cyclic Metalloporphyrin Dimers: Conformational Flexibility, Applications and Future Prospects. *Coord. Chem. Rev.* **2020**, *405*, 213117. (i) Gholami, H.; Chakraborty, D.; Zhang, J.; Borhan, B. Absolute Stereochemical Determination of Organic Molecules through Induction of Helicity in Host−Guest Complexes. *Acc. Chem. Res.* **2021**, *54*, 654−667.

(4) For examples of artificial receptors composed of more than three porphyrin units, see: (a) Fujita, N.; Biradha, K.; Fujita, M.; Sakamoto, S.; Yamaguchi, K. A Porphyrin Prism: Structural Switching Triggered by Guest Inclusion. *Angew. Chem., Int. Ed.* **2001**, *40*, 1718−1721. (b) Tashiro, S.; Kobayashi, M.; Fujita, M. Folding of an Ala-Ala-Ala Tripeptide into a *β*-Turn Via Hydrophobic Encapsulation. *J. Am. Chem. Soc.* **2006**, *128*, 9280−9281. (c) Gil-Ramírez, G.; Karlen, S. D.; Shundo, A.; Porfyrakis, K.; Ito, Y.; Briggs, G. A. D.; Morton, J. J. L.; Anderson, H. L. A Cyclic Porphyrin Trimer as a Receptor for Fullerenes. *Org. Lett.* **2010**, *12*, 3544−3547. (d) Song, J.; Aratani, N.; Shinokubo, H.; Osuka, A. A Porphyrin Nanobarrel That Encapsulates C_{60}. *J. Am. Chem. Soc.* **2010**, *132*, 16356−16357. (e) Meng, W.; Breiner, B.; Rissanen, K.; Thoburn, J. D.; Clegg, J. K.; Nitschke, J. R. A Self-Assembled M_8L_6 Cubic Cage That Selectively Encapsulates Large Aromatic Guests. *Angew. Chem., Int. Ed.* **2011**, *50*, 3479−3483. (f) Nakamura, T.; Ube, H.; Miyake, R.; Shionoya, M. A C_{60}-Templated Tetrameric Porphyrin Barrel Complex via Zinc-Mediated Self-Assembly Utilizing Labile Capping Ligands. *J. Am. Chem. Soc.* **2013**, *135*, 18790−18793. (g) Rousseaux, S. A. L.; Gong, J. Q.; Haver, R.; Odell, B.; Claridge, T. D. W.; Herz, L. M.; Anderson, H. L. Self-Assembly of Russian Doll Concentric Porphyrin Nanorings. *J. Am. Chem. Soc.* **2015**, *137*, 12713−12718. (h) Brenner, W.; Ronson, T. K.; Nitschke, J. R. Separation and Selective Formation of Fullerene Adducts within an $M^{II}_8L_6$ Cage. *J. Am. Chem. Soc.* **2017**, *139*, 75−78.

(5) For optically inactive bisporphyrin-based receptors composed of two porphyrins that are linked by a one linker, see: (a) Huang, X. F.; Rickman, B. H.; Borhan, B.; Berova, N.; Nakanishi, K. Zinc Porphyrin Tweezer in Host-Guest Complexation: Determination of Absolute Configurations of Diamines, Amino Acids, and Amino Alcohols by Circular Dichroism. *J. Am. Chem. Soc.* **1998**, *120*, 6185−6186. (b) Sirish, M.; Schneider, H. J. Highly Efficient Complexations of a Porphyrin Dimer with Remarkably Small Differences between Nucleosides and Nucleotides/The Predominance of Stacking Interactions for Nucleic Acid Components. *J. Am. Chem. Soc.* **2000**, *122*, 5881−5882. (c) Kubo, Y.; Ohno, T.; Yamanaka, J.; Tokita, S.; Iida, T.; Ishimaru, Y. Chirality-Transfer Control Using a Heterotopic Zinc(II) Porphyrin Dimer. *J. Am. Chem. Soc.* **2001**, *123*, 12700−12701. (d) Yamaguchi, T.; Ishii, N.; Tashiro, K.; Aida, T. Supramolecular Peapods Composed of a Metalloporphyrin Nanotube and Fullerenes. *J. Am. Chem. Soc.* **2003**, *125*, 13934−13935. (e) Haino, T.; Fujii, T.; Fukazawa, Y. Guest Binding and New Self-Assembly of Bisporphyrins. *J. Org. Chem.* **2006**, *71*, 2572−2580. (f) Li, X.; Tanasova, M.; Vasileiou, C.; Borhan, B. Fluorinated Porphyrin Tweezer: A Powerful Reporter of Absolute Configuration for Erythro and Threo Diols, Amino Alcohols, and Diamines. *J. Am. Chem. Soc.* **2008**, *130*, 1885−1893. For optically-active bisporphyrin-based receptors, see: (g) Crossley, M. J.; Mackay, L. G.; Try, A. C. Enantioselective Recognition of Histidine and Lysine Esters by Porphyrin Chiral Clefts and Detection of Amino-Acid Conformations in the Bound-State. *J. Chem. Soc., Chem. Commun.* **1995**, 1925−1927. (h) Peng, X.; Komatsu, N.; Bhattacharya, S.; Shimawaki, T.; Aonuma, S.; Kimura, T.; Osuka, A. Optically Active Single-Walled Carbon Nanotubes. *Nat. Nanotechnol.* **2007**, *2*, 361−365.

(6) For optically inactive bisporphyrin-based receptors composed of two porphyrins that are linked by two linkers, see: (a) Anderson, H. L.; Sanders, J. K. M. Amine-Template-Directed Synthesis of Cyclic Porphyrin Oligomers. *Angew. Chem., Int. Ed. Engl.* **1990**, *29*, 1400−1403. (b) Tashiro, K.; Aida, T.; Zheng, J. Y.; Kinbara, K.; Saigo, K.; Sakamoto, S.; Yamaguchi, K. A Cyclic Dimer of Metalloporphyrin Forms a Highly Stable Inclusion Complex with C_{60}. *J. Am. Chem. Soc.* **1999**, *121*, 9477−9478. (c) Oliveri, C. G.; Gianneschi, N. C.; Nguyen, S. T.; Mirkin, C. A.; Stern, C. L.; Wawrzak, Z.; Pink, M. Supramolecular Allosteric Cofacial Porphyrin Complexes. *J. Am. Chem. Soc.* **2006**, *128*, 16286−16296. (d) Mondal, P.; Sarkar, S.; Rath, S. P. Cyclic Bis-Porphyrin-Based Flexible Molecular Containers: Controlling Guest Arrangements and Supramolecular Catalysis by Tuning Cavity Size. *Chem. - Eur. J.* **2017**, *23*, 7093−7103. For optically-active bisporphyrin-based receptors, see: (e) Shoji, Y.; Tashiro, K.; Aida, T. Sensing of Chiral Fullerenes by a Cyclic Host with an Asymmetrically Distorted *π*-Electronic Component. *J. Am. Chem. Soc.* **2006**, *128*, 10690−10691. (f) Ema, T.; Ura, N.; Eguchi, K.; Ise, Y.; Sakai, T. Chiral Porphyrin Dimer with a Macrocyclic Cavity for Intercalation of Aromatic Guests. *Chem. Commun.* **2011**, *47*, 6090−6092. (g) Yamamoto, S.; Iida, H.; Yashima, E. Guest-Induced Unidirectional Dual Rotary and Twisting Motions of a Spiroborate-Based Double-Stranded Helicate Containing a Bisporphyrin Unit. *Angew. Chem., Int. Ed.* **2013**, *52*, 6849−6853. (h) Ousaka, N.; Yamamoto, S.; Hayashi, N.; Li, M.-C.; Ho, R.-M.; Yashima, E. Alkali Metal Ion-Enhanced Threading of a Perylenediimide-Bound Polymer Chain through a Double-Stranded Spiroborate Helicate with a Bisporphyrin Unit. *Chem. Lett.* **2017**, *46*, 970−972. (i) Ousaka, N.; Yamamoto, S.; Iida, H.; Iwata, T.; Ito, S.; Hijikata, Y.; Irle, S.; Yashima, E. Water-Mediated Deracemization of a Bisporphyrin Helicate Assisted by Diastereoselective Encapsulation of Chiral Guests. *Nat. Commun.* **2019**, *10*, 1457.

(7) For optically inactive bisporphyrin-based receptors composed of two porphyrins that are linked by more than three linkers, see: (a) Ikeda, A.; Ayabe, M.; Shinkai, S.; Sakamoto, S.; Yamaguchi, K. A Self-Assembled Porphyrin-Based Dimeric Capsule Constructed by a Pd(II)-Pyridine Interaction Which Shows Efficient Guest Inclusion. *Org. Lett.* **2000**, *2*, 3707−3710. (b) Zheng, Y. R.; Zhao, Z. G.; Wang, M.; Ghosh, K.; Pollock, J. B.; Cook, T. R.; Stang, P. J. A Facile Approach toward Multicomponent Supramolecular Structures: Selective Self-Assembly via Charge Separation. *J. Am. Chem. Soc.* **2010**, *132*, 16873−16882. (c) Nakamura, T.; Ube, H.; Shionoya, M. Silver-Mediated Formation of a Cofacial Porphyrin Dimer with the Ability to Intercalate Aromatic. *Angew. Chem., Int. Ed.* **2013**, *52*, 12096−12100. (d) Colomban, C.; Szaloki, G.; Allain, M.; Gómez, L.; Goeb, B.; Salle, M.; Costas, M.; Ribas, X. Reversible C_{60} Ejection from a Metallocage through the Redox-Dependent Binding of a Competitive Guest. *Chem. - Eur. J.* **2017**, *23*, 3016−3022. For optically-active bisporphyrin-based receptors, see: (e) Barry, N. P. E.; Austeri, M.; Lacour, J.; Therrien, B. Highly Efficient NMR Enantiodiscrimination of Chiral Octanuclear Metalla-Boxes in Polar Solvent. *Organometallics* **2009**, *28*, 4894−4897.

(8) For other one-handed spiroborate-based helicates that are linked by a variety of linkages, such as 2,2′-dihydroxy biphenylene,[8a] biphenylene,[8b,c] and 2,2′-bipyridine and its *N*,*N*′-dioxide units,[8d] in the middle, see: (a) Katagiri, H.; Miyagawa, T.; Furusho, Y.; Yashima, E. Synthesis and Optical Resolution of a Double Helicate Consisting of Ortho-Linked Hexaphenol Strands Bridged by Spiroborates. *Angew. Chem., Int. Ed.* **2006**, *45*, 1741−1744. (b) Miwa, K.; Furusho, Y.; Yashima, E. Ion-Triggered Spring-Like Motion of a Double Helicate Accompanied by Anisotropic Twisting. *Nat. Chem.* **2010**, *2*, 444−449. (c) Ousaka, N.; Shimizu, K.; Suzuki, Y.; Iwata, T.; Itakura, M.; Taura, D.; Iida, H.; Furusho, Y.; Mori, T.; Yashima, E. Spiroborate-Based Double-Stranded Helicates: Meso-to-Racemo Isomerization and Ion-Triggered Springlike Motion of the Racemo-Helicate. *J. Am. Chem. Soc.* **2018**, *140*, 17027−17039. (d) Suzuki, Y.; Nakamura, T.; Iida, H.; Ousaka, N.; Yashima, E. Allosteric Regulation of Unidirectional Spring-Like Motion of Double-Stranded Helicates. *J. Am. Chem. Soc.* **2016**, *138*, 4852−4859. For *meso*- and *racemo*-double-stranded titanium(IV) helicates, see: (e) Ousaka, N.; Itakura, M.; Nagasaka, A.; Ito, M.; Hattori, T.; Taura, D.; Ikai, T.; Yashima, E. Water-Mediated Reversible Control of Three-State Double-Stranded Titanium(IV) Helicates. *J. Am. Chem. Soc.* **2021**, *143*, 4346−4358. Some of the enantiopure spiroborate helicates showed a unique unidirectional spring-like motion upon the binding and release of metal ions[8b−d] or protons.[8d]

(9) For examples of single- and double-helical oligomers and polymers that can encapsulate guest molecules within their inner cavities, see: (a) Prince, R. B.; Barnes, S. A.; Moore, J. S. Foldamer-

https://doi.org/10.1021/acs.joc.1c01155
J. Org. Chem. 2021, 86, 10501−10516

Based Molecular Recognition. *J. Am. Chem. Soc.* **2000**, *122*, 2758−2762. (b) Garric, J.; Léger, J. M.; Huc, I. Molecular Apple Peels. *Angew. Chem., Int. Ed.* **2005**, *44*, 1954−1958. (c) Kumaki, J.; Kawauchi, T.; Okoshi, K.; Kusanagi, H.; Yashima, E. Supramolecular Helical Structure of the Stereocomplex Composed of Complementary Isotactic and Syndiotactic Poly(methyl methacrylate)s as Revealed by Atomic Force Microscopy. *Angew. Chem., Int. Ed.* **2007**, *46*, 5348−5351. (d) Waki, M.; Abe, H.; Inouye, M. Translation of Mutarotation into Induced Circular Dichroism Signals through Helix Inversion of Host Polymers. *Angew. Chem., Int. Ed.* **2007**, *46*, 3059−3061. (e) Kawauchi, T.; Kumaki, J.; Kitaura, A.; Okoshi, K.; Kusanagi, H.; Kobayashi, K.; Sugai, T.; Shinohara, H.; Yashima, E. Encapsulation of Fullerenes in a Helical PMMA Cavity Leading to a Robust Processable Complex with a Macromolecular Helicity Memory. *Angew. Chem., Int. Ed.* **2008**, *47*, 515−519. (f) Pfukwa, R.; Kouwer, P. H. J.; Rowan, A. E.; Klumperman, B. Templated Hierarchical Self-Assembly of Poly(*p*-aryltriazole) Foldamers. *Angew. Chem., Int. Ed.* **2013**, *52*, 11040−11044. (g) Chandramouli, N.; Ferrand, Y.; Lautrette, G.; Kauffmann, B.; Mackereth, C. D.; Laguerre, M.; Dubreuil, D.; Huc, I. Iterative Design of a Helically Folded Aromatic Oligoamide Sequence for the Selective Encapsulation of Fructose. *Nat. Chem.* **2015**, *7*, 334−341.

(10) We could not estimate the binding affinity of $\mathbf{1}_{Na2}$ with **G5** because **G5** is hardly soluble in CH_3CN and $CHCl_3$, whereas **G5** became soluble in CD_3CN in the presence of $\mathbf{1}_{Na2}$ to form a 1:1 inclusion complex after being mixed for 12 h at ambient temperature, as evidenced by its ^{1}H NMR spectral changes with time (Figure S8).

(11) The K_a value of a **G6** analogue bearing the same Tg-bound imide substituent at one end and a bulky 3,5-di-*tert*-butylbenzyl stopper at the other end was almost identical to that of **G6** (ca. 1.1×10^9 M^{-1}).[6h]

(12) **G17** is hardly soluble in CH_3CN but became soluble in CD_3CN in the presence of $\mathbf{1}_{Na2}$, producing a 1:1 inclusion complex (Figure S19).

(13) To avoid the complete racemization of (*M*)-$\mathbf{1}_{TBA2}$ upon heating with **G18**, a 1:1 mixture of (*M*)-$\mathbf{1}_{TBA2}$ and **G18** in CD_3CN that contained a small amount of water (ca. 0.6 equiv) was heated at 70 °C for 114 h and then cooled to ambient temperature before reaching an equilibrium state (Figure 3).

(14) Previously, we reported that the water-mediated racemization of the free (*M*)-$\mathbf{1}_{TBA2}$ at 70 °C was slower than that of its inclusion complex with the less bulky **G4** ((*M*)-$\mathbf{1}_{TBA}$**2**⊃**G4**),[6i] which is different from the present results. The reason for this is unclear at present but is considered to be due to the hydrophobic and bulky 3,5-di-*tert*-butylbenzyl substituents of **G18**, which may prevent the access of water molecules to the spiroborate groups once they are encapsulated into the helicate.

(15) For pacman bisporphyrins that are anchored by a single rigid pillar or spacer, see: (a) Chang, C. K.; Abdalmuhdi, I. Anthracene Pillared Cofacial Diporphyrin. *J. Org. Chem.* **1983**, *48*, 5388−5390. (b) Collman, J. P.; Hutchison, J. E.; Lopez, M. A.; Tabard, A.; Guilard, R.; Seok, W. K.; Ibers, J. A.; L'Her, M. Synthesis and Characterization of a Superoxo Complex of the Dicobalt Cofacial Diporphyrin $[(\mu\text{-}O_2)Co_2(DPB)(1,5\text{-diphenylimidazole})_2][PF_6]$, the Structure of the Parent Dicobalt Diporphyrin $Co_2(DPB)$, and a New Synthesis of the Free-Base Cofacial Diporphyrin $H_4(DPB)$. *J. Am. Chem. Soc.* **1992**, *114*, 9869−9877. (c) Chang, C. J.; Loh, Z. H.; Shi, C. N.; Anson, F. C.; Nocera, D. G. Targeted Proton Delivery in the Catalyzed Reduction of Oxygen to Water by Bimetallic Pacman Porphyrins. *J. Am. Chem. Soc.* **2004**, *126*, 10013−10020. (d) Pognon, G.; Boudon, C.; Schenk, K. J.; Bonin, M.; Bach, B.; Weiss, J. Electrochemically Triggered Open and Closed Pacman Bis-Metalloporphyrins. *J. Am. Chem. Soc.* **2006**, *128*, 3488−3489. (e) Rosenthal, J.; Luckett, T. D.; Hodgkiss, J. M.; Nocera, D. G. Photocatalytic Oxidation of Hydrocarbons by a Bis-Iron(III)-μ-Oxo Pacman Porphyrin Using O_2 and Visible Light. *J. Am. Chem. Soc.* **2006**, *128*, 6546−6547. (f) Givaja, G.; Volpe, M.; Leeland, J. W.; Edwards, M. A.; Young, T. K.; Darby, S. B.; Reid, S. D.; Blake, A. J.; Wilson, C.; Wolowska, J.; McInnes, E. J. L.; Schröder, M.; Love, J. B. Design and Synthesis of Binucleating Macrocyclic Clefts Derived from Schiff-Base Calixpyrroles. *Chem. - Eur. J.* **2007**, *13*, 3707−3723. (g) Ghosh, S. K.; Patra, R.; Rath, S. P. Synthesis and Characterization of anti-bisFe(III) Porphyrins, syn-bisFe(III)-μ-Oxo Porphyrin, and syn-bisFe(III)- μ-Oxo Porphyrin Cation Radical. *Inorg. Chem.* **2010**, *49*, 3449−3460. (h) Leeland, J. W.; White, F. J.; Love, J. B. Encapsulation of a Magnesium Hydroxide Cubane by a Bowl-Shaped Polypyrrolic Schiff Base Macrocycle. *J. Am. Chem. Soc.* **2011**, *133*, 7320−7323. (i) Pan, Q. J.; Odoh, S. O.; Schreckenbach, G.; Arnold, P. L.; Love, J. B. Theoretical Exploration of Uranyl Complexes of a Designed Polypyrrolic Macrocycle: Structure/Property Effects of Hinge Size on Pacman-Shaped Complexes. *Dalton Trans.* **2012**, *41*, 8878−8885.

(16) Mahadevi, A. S.; Sastry, G. N. Cation−π Interaction: Its Role and Relevance in Chemistry, Biology, and Material Science. *Chem. Rev.* **2013**, *113*, 2100−2138.

(17) Such a pacman structure could not be clearly detected by recorded the low-temperature ^{1}H NMR spectra of $\mathbf{1}_{BTMA2}$ in CD_3CN, even at −40 °C.

(18) Hunter, C. A.; Sanders, J. K. M. The Nature of π-π Interactions. *J. Am. Chem. Soc.* **1990**, *112*, 5525−5534.

(19) Elstner, M.; Porezag, D.; Jungnickel, G.; Elsner, J.; Haugk, M.; Frauenheim, T.; Suhai, S.; Seifert, G. Self-Consistent-Charge Density-Functional Tight-Binding Method for Simulations of Complex Materials Properties. *Phys. Rev. B: Condens. Matter Mater. Phys.* **1998**, *58*, 7260−7268.

(20) Eichkorn, K.; Weigend, F.; Treutler, O.; Ahlrichs, R. Auxiliary Basis Sets for Main Row Atoms and Transition Metals and Their Use to Approximate Coulomb Potentials. *Theor. Chem. Acc.* **1997**, *97*, 119−124.

(21) We located the two cationic $BTMA^+$ molecules on both sides of the helicate $\mathbf{1}^{2-}$ to stably simulate the binding process. Locating $BTMA^+$ on only one side of the helicate induced an unbalanced charge distribution in the system, which caused problems in the convergence of the iteration of SCC by DFTB. Therefore, we neutralized the helicate $\mathbf{1}^{2-}$ using two $BTMA^+$ molecules. The binding energy (E_{bind}) of $BTMA^+$ toward the $\mathbf{1}_{(BTMA)2}$ helicate was then calculated by RI-DFT (see Section 5.2 in the Supporting Information).)

(22) Upon mixing $\mathbf{1}_{Na2}$ with 0.5 equiv of nonsymmetric **G10**−**G12**, the ^{1}H NMR signals due to the inclusion complexes of $\mathbf{1}_{Na2}$ further split into two sets of signals as a result of the desymmetrization of a pseudo-D_2-symmetric structure of $\mathbf{1}_{Na2}$ via complexation with the nonsymmetric NMI-based guests[6i] (Figures S12−S14).

(23) (a) Kozlowski, P. M.; Wolinski, K.; Pulay, P.; Ye, B. H.; Li, X. Y. GIAO Nuclear Magnetic Shielding Tensors in Free Base Porphyrin and in Magnesium and Zinc Metalloporphyrins. *J. Phys. Chem. A* **1999**, *103*, 420−425. (b) Gomila, R. M.; Quinonero, D.; Rotger, C.; Garau, C.; Frontera, A.; Ballester, P.; Costa, A.; Deya, P. M. Predicting Experimental Complexation-Induced Changes in ^{1}H NMR Chemical Shift for Complexes between Zinc-Porphyrins and Amines Using the Ab Initio/GIAO-HF Methodology. *Org. Lett.* **2002**, *4*, 399−401. (c) Gomila, R. M.; Garau, C.; Frontera, A.; Quinonero, D.; Ballester, P.; Costa, A.; Deya, P. M. Applicability of the ^{1}H NMR Chemical Shifts Computed by the Ab Initio/GIAO-HF Methodology to the Study of Geometrical Features of Zn-Porphyrin Dimers. *Tetrahedron Lett.* **2004**, *45*, 9387−9391. (d) Iwamoto, H.; Hori, K.; Fukazawa, Y. A Model of Porphyrin Ring Current Effect. *Tetrahedron Lett.* **2005**, *46*, 731−734.

(24) Similar approaches have been applied to several supramolecular host−guest systems. For examples, see: (a) Ajami, D.; Iwasawa, T.; Rebek, J. Experimental and Computational Probes of the Space in a Self-Assembled Capsule. *Proc. Natl. Acad. Sci. U. S. A.* **2006**, *103*, 8934−8936. (b) Mugridge, J. S.; Bergman, R. G.; Raymond, K. N. ^{1}H NMR Chemical Shift Calculations as a Probe of Supramolecular Host−Guest Geometry. *J. Am. Chem. Soc.* **2011**, *133*, 11205−11212.

(25) For a review of chemical shift nonequivalence in prochiral groups, see: Jennings, W. B. Chemical Shift Nonequivalence in Prochiral Groups. *Chem. Rev.* **1975**, *75*, 307−322.

https://doi.org/10.1021/acs.joc.1c01155
J. Org. Chem. 2021, 86, 10501−10516

(26) Samudrala, R.; Zhang, X.; Wadkins, R. M.; Mattern, D. L. Synthesis of a non-cationic, water-soluble perylenetetracarboxylic diimide and its interactions with G-quadruplex-forming DNA. *Bioorg. Med. Chem.* **2007**, *15*, 186−193.
(27) Guha, S.; Goodson, F. S.; Roy, S.; Corson, L. J.; Gravenmier, C. A.; Saha, S. Electronically Regulated Thermally and Light-Gated Electron Transfer from Anions to Naphthalenediimides. *J. Am. Chem. Soc.* **2011**, *133*, 15256−15259.
(28) Alvey, P. M.; Reczek, J. J.; Lynch, V.; Iverson, B. L. A Systematic Study of Thermochromic Aromatic Donor−Acceptor Materials. *J. Org. Chem.* **2010**, *75*, 7682−7690.
(29) Grunder, S.; Torres, D. M.; Marquardt, C.; Błaszczyk, A.; Krupke, R.; Mayor, M. Synthesis and Optical Properties of Molecular Rods Comprising a Central Core-Substituted Naphthalenediimide Chromophore for Carbon Nanotube Junctions. *Eur. J. Org. Chem.* **2011**, *2011*, 478−496.

https://doi.org/10.1021/acs.joc.1c01155
J. Org. Chem. 2021, 86, 10501−10516